

# JGR Solid Earth

## RESEARCH ARTICLE

10.1029/2018JB016986

### Key Points:

- Develop a generalized modeling framework evaluating earthquake volume balance considering seismic deformation, landslide erosion, and erosion-induced isostacy
- Comprehensively evaluate earthquake volume balance across varying topographic and seismotectonic conditions
- Find the overall topographic effect of earthquake cycles in the eastern Tibetan region to be constructive

### Correspondence to:

G. Li,  
ligengeo@gmail.com;  
ligen@caltech.edu

### Citation:

Li, G., West, A. J., & Qiu, H. (2019). Competing effects of mountain uplift and landslide erosion over earthquake cycles. *Journal of Geophysical Research: Solid Earth*, 124. <https://doi.org/10.1029/2018JB016986>

Received 13 JAN 2018

Accepted 3 APR 2019

Accepted article online 9 APR 2019

## Competing Effects of Mountain Uplift and Landslide Erosion Over Earthquake Cycles

Gen Li<sup>1,2</sup> , A. Joshua West<sup>1</sup> , and Hongrui Qiu<sup>1</sup> 

<sup>1</sup>Department of Earth Sciences, University of Southern California, Los Angeles, California, USA, <sup>2</sup>Now at Division of Geological and Planetary Sciences, California Institute of Technology, Pasadena, California, USA

**Abstract** Large earthquakes can construct mountainous topography by inducing rock uplift but also erode mountains by causing landslides. Observations following the 2008 Wenchuan earthquake show that landslide volumes in some cases match seismically induced uplift, raising questions about how the actions of individual earthquakes accumulate to build topography. Here we model the two-dimensional surface displacement field generated over a full earthquake cycle accounting for coseismic deformation, postseismic relaxation, landslide erosion, and erosion-induced isostatic compensation. We explore the related volume balance across different seismotectonic and topographic conditions and revisit the Wenchuan case in this context. The ratio ( $\Omega$ ) between landslide erosion and uplift is most sensitive to parameters determining landslide volumes (particularly earthquake magnitude  $M_w$ , seismic energy source depth, and failure susceptibility, as well as the seismological factor responsible for triggering landslides), and is moderately sensitive to the effective elastic thickness of lithosphere,  $T_e$ . For a specified magnitude, more erosive events (higher  $\Omega$ ) tend to occur at shallower depth, in thicker- $T_e$  lithosphere, and in steeper, more landslide-prone landscapes. For given landscape and seismotectonic conditions, the volumes of both landslides and uplift to first order positively scale with  $M_w$  and seismic moment  $M_o$ . However, higher  $M_w$  earthquakes generate lower landslide and uplift volumes per unit  $M_o$ , suggesting lower efficiency in the use of seismic energy to drive topographic change. With our model, we calculate the long-term average seismic volume balance for the eastern Tibetan region and find that the net topographic effect of earthquakes in this region tends to be constructive rather than erosive. Overall, destructive events are rare when considering processes over the full earthquake cycle, although they are more likely if only considering the coseismic volume budget (as was the case for the 2008 Wenchuan earthquake where landsliding substantially offset coseismic uplift). Irrespective of the net budget, our results suggest that the erosive power of earthquakes plays an important role in mountain belt evolution, including by influencing structures and spatial patterns of deformation, for example affecting the wavelength of topography.

### 1. Introduction

Mountain ranges are among the most conspicuous landforms at the Earth's surface, and they have global-scale effects including on atmospheric circulation (Avouac, 2007; Boos & Kuang, 2010; Molnar & England, 1990) and the long-term carbon cycle (Galy et al., 2007; Raymo et al., 1988; Torres et al., 2014). The geological processes that build mountainous topography have remained hotly debated (e.g., Avouac, 2007; Clark & Royden, 2000; Elliott et al., 2016; Kelsey, 1990; Tapponnier et al., 2001; Whipple et al., 2016). At collisional plate boundaries, thrust-faulting earthquakes are thought to be a major driver of mountain uplift via repeated vertical displacement (e.g., Avouac, 2007; Meade, 2010). However, large earthquakes also cause widespread landslides that collectively generate large volumes of clastic sediment and facilitate erosion of mountains (Hovius et al., 2011; Keefer, 1994; Li et al., 2016; Tanyaş et al., 2017; Wang et al., 2015). Observations from the 2008  $M_w$ 7.9 Wenchuan earthquake revealed that in some cases, the volume of earthquake-triggered landslides can be comparable to or even exceed that of coseismically induced rock uplift (Li et al., 2014; Parker et al., 2011), demonstrating the significant erosive power of large earthquakes and raising fundamental questions about how seismotectonic activity builds mountainous topography.

These observations from Wenchuan, and similar work focused on the 1999 Chi-Chi event (Hovius et al., 2011), have stimulated efforts to develop a generalized understanding of earthquake volume balance, that

is, the balance between earthquake-induced uplift and landslide erosion. Recent studies by Li et al. (2014) and Marc, Hovius, and Meunier (2016) considered how this “coseismic” balance might vary for earthquakes of different magnitude ( $M_w$ ), using models for coseismic uplift and landslide erosion as a function of  $M_w$  (e.g., Cohen, 1996; Keefer 1994; Leonard, 2010; Marc, Hovius, Meunier, Gorum, et al., 2016; Malamud et al., 2004; Wells & Coppersmith, 1994). Marc, Hovius, and Meunier (2016) additionally showed that other factors modulating the total volume of earthquake-triggered landslides, for example, landscape steepness and seismic energy source depth, influence the overall volume balance of a single event. Understanding the role of earthquakes in mountain building requires systematically quantifying these dependencies, since the cumulative work of multiple earthquakes contributes to building topography. However, topography responds not only to coseismic processes (uplift and landsliding), as considered in the work of Li et al. (2014) and Marc, Hovius, and Meunier (2016), but also to postseismic relaxation following coseismic deformation and isostatic compensation to erosional mass removal (Huang et al., 2014; King et al., 1988; Molnar, 2012; Watts, 2001). Interseismic processes may also play important roles (Cattin & Avouac, 2000; Dal Zilio et al., 2019; Godard et al., 2004, 2009; Vergne et al., 2001).

Previous studies have quantified the effects of earthquake cycle processes using physical solutions for the mechanical behavior of dip-slip fault systems with layered structures of different rheological properties (e.g., Cattin & Avouac, 2000; Dal Zilio et al., 2019; King et al., 1988; Simpson, 2014). These studies have been able to describe how first-order topographic forms can emerge from repeated earthquake sequences, but they lacked quantitative constraints on earthquake-triggered erosion. This gap can be filled by recent understanding of the earthquake balance problem (Hovius et al., 2011; Li et al., 2014; Marc, Hovius, & Meunier, 2016; Parker et al., 2011), informed by models describing landslide volumes (Marc, Hovius, Meunier, Gorum, et al., 2016) and observations that landslides are a dominant contributor to orogenic erosion (Keefer, 1994; Li et al., 2017; Malamud et al., 2004). Using this foundation to constrain the erosional term in models akin to that developed by King et al. (1988) promises a holistic, seismologically based description of topographic growth associated with seismic activity and affords the opportunity for a more complete consideration of the volume balance problem over full earthquake cycles. Such an approach is specifically targeted at resolving questions about the role of earthquakes in building topography, that is, as expected in settings with high seismic coupling, recognizing that in other settings aseismic processes may also contribute significantly to topographic development (e.g., Vita-Finzi, 2000).

In the present study, we develop a generalized model building on the framework of King et al. (1988) and parameterizing erosion based on a seismological description of landslide volume (Marc, Hovius, Meunier, Gorum, et al., 2016). This model simulates the two-dimensional (2-D) surface displacement field caused by seismic processes over full earthquake cycles, focusing on the end-member case where interseismic tectonic loading occurs in the far field and causes minimal transient deformation of the fault zone, as may be the case along the eastern margin of the Tibetan Plateau (see below). We consider that future work could extend our framework to consider settings where interseismic loading is important. As developed here, our model allows us to (i) test the sensitivity to relevant seismological and topographic parameters; (ii) distinguish the role of coseismic deformation, postseismic relaxation, landslide erosion, and erosional unloading-induced isostatic response; and (iii) evaluate how different processes affect the spatial patterns of mass redistribution and thus general topographic form. We are further able to reevaluate the question of earthquake volume balance across events of different magnitudes, specifically considering the importance of assumptions about the seismological factors most responsible for landslide triggering as well as the importance of the spatial window over which volume balance is calculated (e.g., Densmore et al., 2012). We can evaluate the efficiency of seismic processes in doing geomorphic work, in other words how much of the released seismic moment converts to uplifting or eroding topography, as well as the relative importance of earthquake events with varying magnitudes in the total volume budget. Finally, we contextualize these model results by presenting an analysis of how the volume balance for the Wenchuan event depends on the spatial integration boundaries and seismotectonic conditions. In the context of the Wenchuan event, we model the long-term volume balance over multiple seismic cycles to examine the role of earthquakes in mountain belt evolution at the eastern margin of the Tibetan Plateau. This paper thus links seismicity to landscape evolution, promising better understanding of how fault systems and associated earthquake cycles drive orogenic growth.

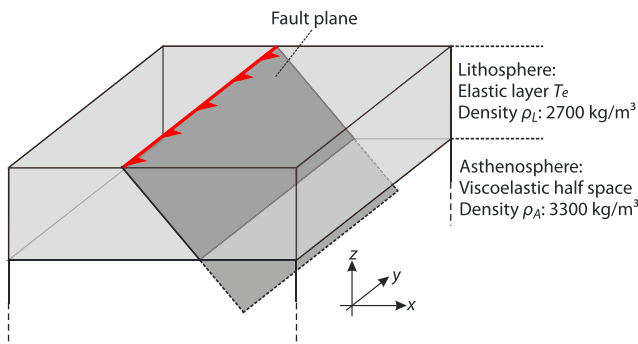


**Figure 1.** Illustrated diagram of the fault setting modeled in this study, composed of elastic lithosphere with thickness  $T_e$  and density  $\rho_L$ , viscoelastic asthenosphere with density  $\rho_A$ , and a thrust fault plane with dip  $\theta$ . The fault plane is assumed to be large enough to accommodate all earthquake magnitudes of interest (up to  $M_w$  8–9 in this context), and the rupture dimensions are determined from  $M_w$ -based scaling relations for dip-slip fault earthquakes (Leonard, 2010, Table 6).

and fault displacement are determined using empirical scaling relations with earthquake magnitude  $M_w$  (Leonard, 2010). All earthquakes rupture to the surface, and the depth of an earthquake event is at the bottom of the rupture plane and determined as the product of rupture width and  $\sin(\theta)$ . To allow an extensive exploration of earthquakes of different magnitudes, we assume that the fault plane is large enough to accommodate earthquakes over a wide range of magnitudes (up to  $M_w = 8$ –9 in this study). We acknowledge that, because earthquake depth varies as a function of  $M_w$  and is independent of  $T_e$ , there are scenarios in our model when earthquakes occur at depth deeper than the conventional seismogenic zone. Whether these scenarios are physically realistic is debatable. Although it is widely accepted that earthquakes mostly occur in the seismogenic zone (e.g., Scholz, 2002), recent studies (Jiang & Lapusta, 2016) suggest that large earthquakes can rupture deeper than the seismogenic zone, as the deeper fault extensions into the creeping zone may dynamically localize and weaken under seismically induced shear heating and strain rate effects. Validating the deep penetration of large earthquakes is beyond the scope of this study, as our main purpose is to provide a setting where the effects of relevant parameters (e.g.,  $T_e$ ) can be fully explored. Thus, in our model, we allow earthquakes to occur at depth independent of  $T_e$ , recognizing that some deep-penetrating events may or may not be physically realistic—but also realizing that the deepest earthquakes are likely to be least relevant to landslide triggering (see below). This setting allows us to use a computational simple analytical solution that approximates postseismic deformation (Savage & Gu, 1985).

## 2.2. Processes Operating Over Earthquake Cycles

Our modeling framework accounts for tectonic uplift, landslide erosion, and erosion-induced isostatic compensation over full earthquake cycles. Tectonic uplift is driven by interseismic loading and expressed as seismic and aseismic deformation (Avouac, 2007; Cattin & Avouac, 2000; King et al., 1988; Simpson, 2015). The seismic component of deformation is a combination of the deformation caused by strain release during earthquakes (coseismic) and the corresponding lithospheric rheological adjustment (postseismic relaxation and isostatic response to coseismic deformation) over interseismic periods (King et al., 1988; Simpson, 2015). Aseismic deformation is conceptualized as ductile creeping and loading along the fault plane at a relatively constant long-term rate (Savage, 1983; Simpson, 2015). Landslides are triggered coseismically, and landslide debris is gradually removed out of mountain ranges by rivers between earthquake cycles (Croissant et al., 2017; Hovius et al., 2011; Wang et al., 2015). This landslide-induced erosional unloading causes isostatic response, which operates over interseismic time periods and works to compensate volume loss (Molnar, 2012). These processes are all time-dependent; for example, export of landslide-derived sediment and isostatic response are not instantaneous but occur over time scales of thousands of years or longer. In our model, the overall volume budget of these processes is calculated after multiple earthquake cycles (greater than thousands of years to Myr) to reflect time scales relevant to mountain belt evolution, so we consider only the “end state” and ignore any path dependency. For computational simplicity and efficiency, we make five further major approximations and simplifications.

## 2. Model Summary, Approximations, and Simplifications

Here we summarize our model setting, framework, and the major assumptions and simplifications taken in this work.

### 2.1. Fault Implementation

We model the lithosphere-asthenosphere system (Figure 1) as an elastic plate (thickness  $T_e$ , density  $\rho_L$ , 2,700 kg/m<sup>3</sup>, Young's modulus  $E$  70 GPa, Poisson ratio  $\nu$  0.25) overlying a viscoelastic half space (density  $\rho_A$  3,300 kg/m<sup>3</sup>). Following King et al. (1988), the fault is implemented as a plane (dip  $\theta$ ) extending through the elastic plate into the viscoelastic half space. The upper part of the fault in the lithosphere behaves in an elastic-brittle manner during earthquake ruptures, whereas the lower part of the fault in the viscoelastic half space is set to be ductile over the long term, but acts similarly as the upper part in an elastic-brittle fashion when earthquakes occur (as in King et al., 1988). In our model, we consider that all earthquake events rupture to the surface, and the rupture dimensions

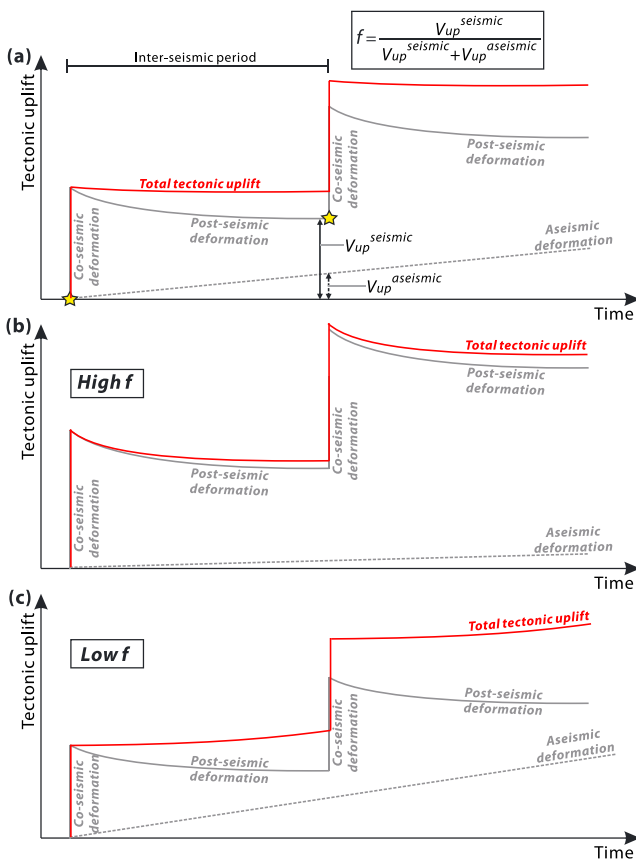


**Figure 2.** Schematic diagrams of seismic and aseismic deformation of the fault zone over earthquake cycles, the meaning of factor  $f$ , and two cases of high and low  $f$ . (a) Tectonic uplift versus time in the context of earthquake cycles: total tectonic uplift (red solid curve) is composed of coseismic (gray solid line, occurring during earthquakes represented by the yellow stars), postseismic (gray solid curve), and aseismic (gray dashed curve) deformations. (b) Tectonic uplift versus time in a high  $f$  case where seismic deformation contributes most to total uplift, that is, high interseismic coupling as observed in the Himalayas (Stevens & Avouac, 2015). (c) Tectonic uplift versus time in a low  $f$  case where aseismic uplift is significant. Note that these schematic diagrams are for regional loading scenarios where interseismic deformation at the fault zone is neglected, whereas in localized loading scenarios deformation may show different trends over time (e.g., Cattin & Avouac, 2000; Simpson, 2015).

finite length. Notably, King et al. (1988) show that when applying 2-D flexural isostacy models to settings with finite strike extent, the results are accurate within a few percent if fault length is about 10 times of  $T_e$ . High-magnitude earthquakes should satisfy this rule; for example, a  $M_w8$  reverse fault-earthquake(surface rupture length  $\sim 270$  km, according to the  $M_w$ -fault dimension scaling relation in Leonard, 2010) occurring in a region with a common  $T_e$  value of 20 km (Burov & Diamant, 1995; Fielding & McKenzie, 2012; Jordan & Watts, 2005; Maggi et al., 2000). Applying 2-D approaches to single, smaller-magnitude earthquakes with shorter fault length may cause larger uncertainties. However, the cumulative deformation of these smaller-magnitude events over multiple earthquake cycles may make them suitable for using 2-D models. Specifically, if each smaller event ruptures a different segment of a fault (e.g., the Himalayan main thrust-front; Bollinger et al., 2014), over the long term, the rupture length of each smaller event can add up to reach the full fault length. This scenario can be demonstrated quantitatively, by comparing the cumulative rupture length to the fault length, or the rupture length of the maximum-magnitude event. To do this, we can use the recurrence time of earthquakes of different magnitudes using the Gutenberg-Richter frequency-magnitude relation (Gutenberg & Richter, 1954):

First, we simplify the effect of interseismic tectonic loading and aseismic slip. Specifically, our model reflects an end-member case which minimizes interseismic tectonic loading. The effects of loading on the fault zone depend on its mechanism and spatial scale (Cattin & Avouac, 2000; Johnson, et al., 2005; Simpson, 2015). Finite element modeling of time-dependent viscoelastic deformation shows that when interseismic loading is applied from far field at regional scales, there is negligible influence on surface vertical deformation (Simpson, 2015). In this scenario, coseismic deformation and postseismic relaxation should accurately describe vertical deformation over earthquake cycles. Our model represents this scenario, for example, in the Longmen Shan Mountains at the eastern margin of the Tibetan Plateau where the Wenchuan earthquake occurred but limited active shortening was observed before the earthquake (Burchfiel et al., 2008; Zhang et al., 2004). For regions where interseismic loading operates at scales comparable to fault dimensions (e.g., creeping at the fault root below the locking depth) and causes significant surface deformation (e.g., Taiwan and the frontal Himalayas; Cattin & Avouac, 2000; Johnson et al., 2005; Stevens & Avouac, 2015), our model can only constrain the coseismic and postseismic components and the related volume balance, but lacks the interseismic component related to loading. Future work could add modeling of these interseismic processes (e.g., Cattin & Avouac, 2000; Dal Zilio et al., 2019; Simpson, 2015) into our framework, but is beyond the scope of this study.

Besides tectonic loading, we also simplify the influence of aseismic slip during the interseismic time period by introducing a deformation partitioning coefficient  $f$  that quantifies the proportion of seismically versus aseismically induced deformations over earthquake cycles (section 3.1 and see Figure 2). We explicitly distinguish this aseismic component because our main goal is to investigate topographic development by seismic processes, and for our purposes, the main distinction is that aseismic processes do not directly trigger landslides while seismic processes do.

Second, we calculate the two-dimensional (2-D) deformation fields using analytical solutions that are originally derived for faults with infinite length (Cohen, 1996; King et al., 1988; Savage & Gu, 1985, and references therein). Such 2-D approaches to model seismic deformations have been applied to several fault-impacted landscapes, for example, the western and central United States and Taiwan, and to subduction zones in Japan (e.g., Johnson et al., 2005; Savage & Gu, 1985; Stein et al., 1988).

However, 2-D approaches may lead to uncertainties for real faults with

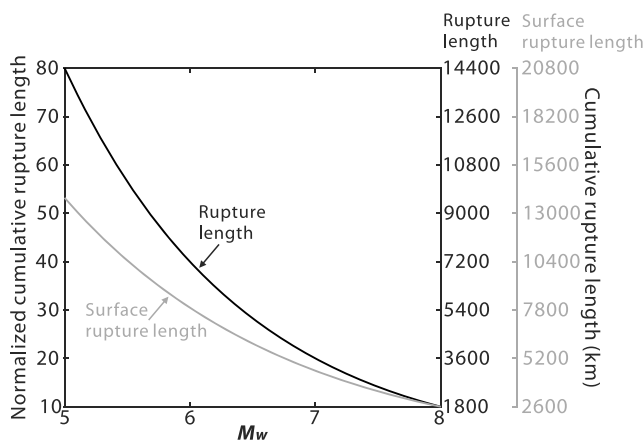


**Figure 3.** Cumulative rupture length as a function of earthquake magnitude over  $10 M_w 8$  earthquake cycles, showing rupture length (subsurface) and surface rupture length. The normalized cumulative rupture length is normalized by the rupture length of one single maximum magnitude ( $M_w = 8$  in this case) event, which is assumed to be equivalent to the full fault length. Smaller-magnitude earthquakes rupture different segments of the fault. Rupture length is calculated using the  $M_w$ -based empirical scaling relationships for dip-slip fault earthquakes reported in Leonard (2010).

1984; Savage & Gu, 1985). Although this time scale may exceed one earthquake cycle, it is well within the range of our time scale of interest over multiple earthquake cycles (thousand years to Myr), so we argue that postseismic deformation can be considered as (near)complete in our modeling framework. The (near)complete assumption also allows us to take advantage of the analytical solution derived by Savage and Gu (1985), who take a plate flexure approach to approximate the complete time-dependent relaxed-asthenosphere solution of Thatcher and Rundle (1984).

Fourth, we assume coseismic landsliding and subsequent fluvial removal of landslide debris are the major mechanisms by which earthquakes drive erosion, and we neglect transient changes in landslide propensity and landscape erodibility caused by seismic processes in postearthquake time periods. Recent studies show that in seismically active landscapes, material strength and its spatiotemporal variations are important in determining spatial and temporal patterns of landslide occurrence (Gallen et al., 2015; Marc et al., 2015; Scheingross et al., 2013). Material strength is a complex function of geological, climatic, and seismotectonic conditions. Earthquakes can alter strength, thus modulating landslide propensity and landscape erodibility in postseismic time periods. For example, Scheingross et al. (2013) found that in the San Andreas Fault system, interseismic slow-moving landslides cluster near the creeping section but are rare in earthquake-shock parts, suggesting that earthquakes may preferentially remove weak material via landsliding. Thus, post-earthquake landslide propensity may be decreased in this scenario. Other studies have observed enhanced landsliding rates after large earthquakes (e.g., in Taiwan, Japan, Papua New Guinea, and Sichuan), suggesting a reduction of material strength following earthquakes. Although landsliding rate increases in those settings, the postseismic landslides amount to a limited addition (<10%) to the total coseismic landslide volumes (Fan et al., 2018; Li et al., 2016; Marc et al., 2015; Zhang et al., 2014). Studying landslides caused by two historic earthquakes (1929 and 1968) in New Zealand, Parker et al. (2015) proposed that earthquakes can cause damage in landscapes that persists longer than decadal postearthquake time periods, preconditioning hillslopes for failure in next earthquakes. However, the longer-term (greater than hundreds of years) effects remain unclear. Geophysical surveys suggest that the weakening and recovery of substrate strength occurs relatively rapidly, that is, within around 1–10 years following the main shock, as inferred from changes in seismic velocity (e.g., Brenguier et al., 2008; Gassenmeier et al., 2016). We also acknowledge that earthquakes may affect landscape erodibility (Vanmaercke et al., 2017) and nonlandsliding erosional flux, but we expect a minor influence given the dominant role of landslides in sustaining long-term erosional flux in steep mountains (Hovius et al., 1997; Keefer, 1994; Li et al., 2017; Marc et al., 2019). Overall, we expect that these factors contribute a minor part to the total earthquake-caused erosional budget compared to

$$\log_{10} N = a - b M_w \quad (1)$$

where  $N$  is the number of earthquakes with magnitude  $\geq M_w$  within a defined time period (taken as 100,000 years here) and  $a$  and  $b$  ( $b$  chosen as the global average value, 0.9; Malamud et al., 2004, and references therein) are the scaling parameters. We then calculate the total rupture length, that is, the product of earthquake recurrence time and the rupture length for specified magnitude, for each earthquake magnitude bin ( $\Delta M_w = 0.1$ ). The results (Figure 3) indicate that, over the course of 10 cycles of the maximum-magnitude event (assuming maximum  $M_w = 8$ , rupturing the full fault length), smaller-magnitude earthquakes can produce a total rupture length 10–60 times that of the full fault length, suggesting that cumulatively these smaller events can work to rupture the full fault and form structures with sufficient length to make them suitable to modeling using 2-D approaches.

Third, we assume (near)complete postseismic deformation over multiple earthquake cycles. Real postseismic deformation is time-dependent, and assuming that the asthenosphere behaves as a Maxwell material, a standard time scale metric is the Maxwell relaxation time  $\tau$ , typically around 10–100 years (Johnson et al., 2005; Simpson, 2015). Previous studies assume postseismic deformation approaches completion after ~10–50 $\tau$  (so ~100–5,000 years; e.g., Johnson et al., 2005; Thatcher & Rundle, 1984; Savage & Gu, 1985).

Although this time scale may exceed one earthquake cycle, it is well within the range of our time scale of interest over multiple earthquake cycles (thousand years to Myr), so we argue that postseismic deformation can be considered as (near)complete in our modeling framework. The (near)complete assumption also allows us to take advantage of the analytical solution derived by Savage and Gu (1985), who take a plate flexure approach to approximate the complete time-dependent relaxed-asthenosphere solution of Thatcher and Rundle (1984).

coseismic landslides, but we recognize that they are also important mechanisms by which earthquakes may affect erosion.

Fifth and finally, we assume complete removal of landslide debris between earthquake cycles. This assumption is mainly supported by observations of suspended sediment load and by modeling studies of bed load transport which both show relatively rapid removal of landslide debris compared to typical earthquake return times (Croissant et al., 2017; Hovius et al., 2011; Wang et al., 2015). Notably, a recent modeling study (Croissant et al., 2017) systematically explored a range of controlling factors on landslide evacuation time in postearthquake landscapes, including landslide characteristics (e.g., volume, grain size, landslide dam stability, and connectivity to channels), earthquake magnitude, climatic and hydrologic conditions (e.g., mean runoff and discharge variability), and the properties of the fluvial network (e.g., channel width and steepness). They found that across a wide range of conditions, it is the dynamic narrowing of alluvial channels due to landslide input that plays a key role in prompting postearthquake river transport capacity and setting the landslide evacuation time to be around less than tens to hundreds of years. Some other studies, even without considering the dynamic evolution of channel morphology (e.g., Yanites et al., 2010), also suggest an evacuation time of 100–1,000 years, that is, shorter or comparable to the recurrence time for large earthquakes. The assumption that landslide debris is efficiently evacuated is supported by field observations that mountainous valleys accumulate little clastic sediment (Parker et al., 2011; Marc, Hovius, & Meunier, 2016). However, we recognize that in some settings, such as the central Nepal Himalaya, the relatively short recurrence time for large earthquakes (Bollinger et al., 2014) may lead to persistence of landslide debris within the landscape, violating this assumption. Nonetheless, we approximate seismically induced erosional unloading using the magnitude and pattern of earthquake-triggered landslides. For computational simplicity, we also do not account for the effect of the sedimentation of landslide materials in frontal basins, assuming that all landslide sediment is exported and deposited in further downstream areas with minimal influence on fault zone deformation. In general, sedimentation in footwall basins would reduce both local subsidence due to sediment infilling and adjacent hanging wall uplift due to flexural isostatic response to sediment loading (e.g., Densmore et al., 2012; King et al., 1988). However, explicit modeling the effect of local sedimentation requires constraints on the distribution of sediment in subsidence areas, which could be explored in future studies but is beyond the scope of this study.

These approximations allow us to adopt a set of analytical solutions, making it possible to explore relevant parameter space and in the process gain insight into what controls the volume balance of earthquakes. However, unlike fully resolved numerical models of landscape evolution, we do not attempt to simulate the full suite of factors responsible for time-dependent topographic development. In the following sections, we describe in more detail how we model different processes and related deformation over earthquake cycles.

### 3. Model Setup and Parameterization

#### 3.1. Tectonic Uplift Driven by Coseismic, Postseismic, and Aseismic Deformation

Seismic deformation is expressed as the vertical surface displacement caused by coseismic deformation and postseismic adjustment (King et al., 1988). We model the coseismic displacement field using an analytical solution to a 2-D dip-slip dislocation model (Cohen, 1996). Fault displacement and length are calculated using the empirical scaling relations between earthquake magnitude and average displacement ( $D$ ) and surface rupture length ( $L_{sf}$ ) for dip-slip fault earthquakes, respectively (Leonard, 2010; Table 6). To simulate postseismic relaxation integrated over time scales of greater than hundreds to thousands of years, comparable to the time scales of multiple earthquake cycles, we adopt a computationally convenient, analytical solution of Savage and Gu (1985), who use a plate flexure approach to approximate the complete time-dependent relaxed-asthenosphere solution of Thatcher and Rundle (1984). This postseismic deformation solution represents a viscoelastic gravitational solution (Savage & Gu, 1985, equations (4), (5), and (14)) that accounts for the effect of gravity and the corresponding isostatic adjustment to coseismic deformation (Savage & Gu, 1985; Thatcher & Rundle, 1984). The net seismically induced rock uplift volume ( $V_{up}^{seismic}$ ) is determined as the sum of local subsidence and uplift, and varies as a function of  $\theta$ ,  $T_e$ , and  $M_w$  (Savage & Gu, 1985).

To account for the uplift volume caused by aseismic processes ( $V_{\text{up}}^{\text{aseismic}}$ ) and link this quantity to the seismically uplifted volume, we introduce a partitioning coefficient  $f$ :

$$f = V_{\text{up}}^{\text{seismic}} / (V_{\text{up}}^{\text{aseismic}} + V_{\text{up}}^{\text{seismic}}) \quad (2)$$

where  $f$  is the proportion of seismically induced uplift relative to the total uplift caused by seismic and aseismic deformations over one seismic cycle. By definition,  $f$  is close to 1 in regions with high interseismic coupling (locked faults as in the Himalayas and illustrated in Figure 2b; Stevens & Avouac, 2015), and is much smaller in regions with low coupling (Figure 2c). We later use  $f$  to evaluate how aseismic slip contributes to the volume budget and balance over earthquake cycles (section 7). We consider a scenario where tectonic loading is applied from far field at regional scales and is expected to have negligible influence on near-fault surface deformation during the interseismic period (Simpson, 2015). Thus, as noted above (section 2), in regions where interseismic loading is significant (e.g., Taiwan and the frontal Himalayas), our model can only resolve the coseismic and postseismic components of deformation, and further work to incorporate the interseismic component would be needed to describe a complete seismic cycle.

### 3.2. Seismic Landslide Erosion

#### 3.2.1. Landslide Volume

To describe the total volume of landslides associated with an earthquake event, Marc, Hovius, Meunier, Gorum, et al. (2016) adopt an empirical linear relation between landslide volume and ground motion at local scales, simulate seismic ground motion using the empirical relations reported by Boore and Atkinson (2008), and integrate across landscapes to obtain total landslide volume. This modeling framework has also been used to define the boundaries of landslide occurrence, that is, the spatial extent of landsliding (Marc et al., 2017).

We predict the volume of earthquake-triggered landslides ( $V_{ls}$ ) using the model of Marc, Hovius, Meunier, Gorum, et al. (2016), accounting for seismotectonic and topographic conditions, and further consider the effect of different seismological landslide-triggering factors. Specifically, the landslide volume is calculated as:

$$V_{ls} = \pi \delta_V a_c R_0^2 A_{\text{topo}} \left( \frac{R_{\text{ref}} b \bar{S}}{R_0 a_c} - 1 \right)^2 \left( \frac{L}{I_c} \right) \exp \left( \frac{S_{\text{mod}}}{T_{sv}} \right), \quad (R_{\text{ref}} b \bar{S} > a_c R_0) \quad (3)$$

where  $V_{ls}$  is the volume of earthquake-triggered landslides,  $\delta_V$  is the hillslope material sensitivity to landsliding under a given shaking,  $a_c$  is the landslide-triggering threshold acceleration (0.15 g),  $R_0$  is the mean depth of rupture area as an approximation of the mean depth of seismic energy sources,  $A_{\text{topo}}$  is the proportion of landscape area with sufficient steepness to trigger landsliding,  $b$  is the averaged acceleration at a reference difference  $R_{\text{ref}}$  (taken as 1 km) away from the seismic energy source,  $\bar{S}$  is a coefficient representing the landscape-averaged site effects on amplification (dimensionless),  $L$  is the rupture length of the seismogenic fault as determined from  $M_w$ -based scaling relations for dip-slip faults (Leonard, 2010),  $I_c$  is a constant representing the characteristic length of seismic energy source,  $S_{\text{mod}}$  is the modal slope angle for the studied landscape, and  $T_{sv}$  is the global-averaged steepness normalization constant ( $11.6 \pm 0.6^\circ$ ).

A complete derivation of equation (3) is detailed in Marc, Hovius, Meunier, Gorum, et al. (2016). Here we summarize their approach, emphasizing how they derive local seismic ground motion, a central parameter in the model. Marc, Hovius, Meunier, Gorum, et al. (2016) assume that at local scales, landslide volume per unit area (i.e., “landslide volume density”) scales with an exceedance acceleration, the difference between local ground motion  $a$  and the landslide-triggering threshold acceleration  $a_c$ , following empirical observations (e.g., Meunier et al., 2007). They calculate the patterns of ground motion and landslides caused by one seismic energy point source (conceptualized as a spot with a characteristic length of  $I_c$ ) at depth  $R_0$  across the whole landscape, integrate over the total number of seismic energy point sources ( $L/I_c$ ) and the range of the emission angles and radii of seismic waves, correct for the steepness of landscapes ( $A_{\text{topo}}$  and  $S_{\text{mod}}$ ), and obtain a landslide volume function with scaling parameters  $T_{sv}$  and  $\delta_V$ . They then estimate the scaling parameters ( $T_{sv}$  and  $\delta_V$ ) by calibrating the model to a global database of the volumes of coseismic landslides. Estimating local ground motion is a key part of their analysis. They obtain local seismic peak ground

acceleration  $a$  at one landscape cell caused by a seismic energy point source, assuming that attenuation is mainly caused by geometric spreading of seismic waves and neglecting any nonlinear attenuation, as:

$$a = b(\bar{S} + dS)R_{ref}/d \quad (4)$$

where  $b$  is the source acceleration at a reference distance  $R_{ref}$  (taken as 1 km here),  $\bar{S}$  is the average site response over the whole landscape that accounts for how surface topography modulates seismic acceleration,  $dS$  is the deviation of local site response from the landscape-averaged  $\bar{S}$ , and  $d$  is the distance of the landscape cell to the seismic energy source. Equation (4) thus represents a simplified form of ground motion prediction equations, accounting for scaling with earthquake magnitude, site effects, and distance from the source (e.g., Boore & Atkinson, 2008).

Equation (4) is difficult to solve directly because  $b$ ,  $\bar{S}$ , and  $dS$  are not well constrained at regional scales. Empirical observations and modeling studies show that the local site response of source acceleration depends strongly on hillslope morphology and that  $(\bar{S}+dS)$  can vary significantly, for example, by a factor of 2–10 (e.g., Maufroy et al., 2014; Meunier et al., 2008). Marc, Hovius, Meunier, Gorum, et al. (2016) propose that when integrating over the whole landscape, the total effect of  $dS$  should be negligible (i.e., treating  $dS$  as random noise), considering that landslides occur across multiple locations characterized by randomly varying  $dS$ . After eliminating the  $dS$  term,  $b\bar{S}$  is then considered as a combined term. The term  $b$  is calculated using a group of  $M_w$ -dependent ground motion prediction equations developed by Boore and Atkinson (2008):

$$b\bar{S} = b_{sat}\bar{S} \exp[e_5(M_w - M_h) + e_6(M_w - M_h)^2], \quad (M_w \leq M_h) \quad (5)$$

$$b\bar{S} = b_{sat}\bar{S} \exp[e_7(M_w - M_h)], \quad (M_w > M_h) \quad (6)$$

where  $M_h$  is a “hinge” magnitude beyond which ground motion saturates at  $b_{sat}$  and  $e_5$ ,  $e_6$ , and  $e_7$  are the empirical parameters. These parameters are constants for the 5%-damped pseudo-acceleration (*PSA*) for seismic waves with specified periods or for other ground motion indexes like peak ground accelerations (*PGA*) and peak ground velocities (*PGV*), and are empirically determined from 58 worldwide earthquakes (Boore & Atkinson, 2008).

Although  $b_{sat}$  and  $\bar{S}$  are difficult to determine independently, Marc, Hovius, Meunier, Gorum, et al. (2016) use empirical observations to constrain the combined term  $b_{sat}\bar{S}$ . Neglecting  $dS$ ,  $b_{sat}\bar{S}R_{ref}/d$  should predict the saturated surface ground motion at distance  $d$ . Following this relation, Marc, Hovius, Meunier, Gorum, et al. (2016) suggest that a representative value of  $b_{sat}\bar{S}$  is 4g, because this value means surface peak ground accelerations (*PGA*) around 0.4–0.8 g for large earthquakes with a source depth of 5–10 km, consistent with field observations from the 1999 Chi-Chi and 2008 Wenchuan earthquakes (Lee et al., 2001; Li et al., 2008). We retain this value suggested by Marc, Hovius, Meunier, Gorum, et al. (2016).

In our model, we introduce two modifications of the landslide model by Marc, Hovius, Meunier, Gorum, et al. (2016), to allow examination of landslide-triggering mechanisms and to reduce free parameters. First, we consider a range of seismological factors that can potentially trigger landslides. Marc, Hovius, & Meunier (2016), and Marc, Hovius, Meunier, Gorum, et al. (2016) assume that earthquake triggering of landslides is most directly related to 1 Hz (period = 1 s) seismic *S* waves. However, the property of seismic energy release that causes landslides and thus optimally describes the total volume is not well known. In addition to 1-Hz waves, seismic waves of other frequencies, *PGA*, and peak ground velocities (*PGV*) have all been proposed as best explaining landsliding associated with earthquakes (Athanasopoulos-Zekkos et al., 2016; Dreyfus et al., 2013; Harp & Jibson, 1996; Jibson & Keefer, 1993; Tanyaş et al., 2017). Given this uncertainty, we use the framework of Marc, Hovius, Meunier, Gorum, et al. (2016) to model the volumes of earthquake-triggered landslides assuming different seismic factors that control landsliding triggering. We calculate the ground motion associated with each factor referring to the empirical relations and parameters reported by Boore and Atkinson (2008). For *S* waves, we focus on the oscillator period range of 0.1–10 s, or frequency bands of 0.1–10 Hz, as >10-Hz waves have high-quality decay and <0.1-Hz waves likely have too long wavelength to cause damage at hillslope scales (Marc, Hovius, Meunier, Gorum, et al., 2016). In each case,  $V_{ls}$  is

calculated as a function of  $\delta_{sn}$ ,  $S_{mod}$ ,  $R_0$ , and the seismological landslide-triggering factor that directly determined  $M_h$ ,  $e_5$ ,  $e_6$ , and  $e_7$ .

Second, we combine  $\delta_V$  and  $A_{topo}$  as  $\delta_{sn}$ , the normalized landscape failure susceptibility, to reflect the overall characteristics of a landscape:

$$\delta_{sn} = \frac{\delta_V A_{topo}}{\bar{\delta}_V} \quad (7)$$

where  $\bar{\delta}_V$  is the global average hillslope material sensitivity ( $4,174 \text{ m}^3/\text{km}^2$ , empirically determined from a global landslide inventory; Marc, Hovius, Meunier, Gorum, et al., 2016).  $\delta_{sn}$  thus integrates the effects of the properties of hillslope material and the overall steepness of the studied landscape, normalized by a global average condition.

### 3.2.2. Landslide Spatial Pattern

For the landslide spatial distribution pattern, we adopt an empirical relation (Marc et al., 2017; Meunier et al., 2007) and assume a linear seismic energy source:

$$P_{Vls} = P_0 \frac{R_0}{d} \exp\left(-\frac{d-R_0}{R_0\beta}\right) \quad (8)$$

where  $P_{Vls}$  is the landslide volumetric density (volume of landslides in unit area;  $\text{m}^3/\text{km}^2$ ),  $d$  is the distance to the energy source, and  $P_0$  and  $\beta$  are the scaling factors. Parameter  $\beta$  is defined here as the spatial decay factor, with higher values meaning more widely spread landsliding. Note that equation (7) is analogous to the law of seismic wave attenuation accounting for both geometric spreading and quality decay, and has successfully reproduced the patterns of landslides caused by the Chi-Chi, Northridge, Finisterre, and Wenchuan earthquakes (Li, Zhang, et al., 2018; Meunier et al., 2007). Based on current studies,  $1/\beta$  ranges from around 0 (Chi-Chi) to 5 (Northridge). We assume landslide erosion results in complete removal of material within an earthquake cycle (Parker et al., 2011) and for simplicity do not consider the effects of sedimentation in adjacent basins, which will influence spatial patterns and could be added in future work (see Section 2.2).

### 3.3. Isostatic Uplift

Using a flexural-isostasy model, we model the isostatic responses as the flexure due to erosional unloading (King et al., 1988; Watts, 2001). Landslide-induced erosion is converted to erosion depth across a 2-D cross section and approximated as a series of linear unloads, and the flexure caused by each segment of unloading is calculated numerically, after King et al. (1988). The rationale of using this 2-D approach is discussed in section 2.1.

At local scales, the volume of erosion-induced isostatic uplift ( $V_{up}^{isostasy}$ ) varies as a function of landslide volume,  $T_e$ , and the landslide spatial decay factor,  $\beta$ . We note that, in this context,  $V_{up}^{isostasy}$  only refers to the isostatic response to erosion, following the convention of King et al. (1988). There is also isostatic response to seismic deformation over full earthquake cycles, but this component is considered in the calculation of postseismic deformation, thus in the term  $V_{up}^{seismic}$  (section 3.1; Savage & Gu, 1985, and references therein).

As noted above, fluvial evacuation of landslide debris out of mountains (erosional unloading) and the isostatic response do not occur instantaneously, but operate over interseismic periods (Hovius et al., 2011; Wang et al., 2015). Thus,  $V_{up}^{isostasy}$  is calculated at the end of multiple seismic cycles when landslide evacuation and isostatic adjustment are complete, the same stage when postseismic deformation is (almost) complete and accounted for in our calculation (sections 2.2 and 3.1).

### 3.4. Selection of Spatial Window

Previous studies show that seismically induced deformations and erosion vary spatially (Hovius et al., 2011; King et al., 1988; Keefer, 1994; Li et al., 2014; Marc, Hovius, Meunier, Gorum, et al., 2016; Parker et al., 2011); thus, the total balance between uplifted and eroded volume depends on the spatial window over which the volumes are budgeted. To account for this effect, we explore a wide range of values for the width of this window, and we focus on two representative cases in our discussion: (1) a “near-field window” on the hanging wall where most coseismic uplift and earthquake-triggered landslide erosion occur, with the width of this

window ( $W_n$ ) determined by the distance beyond which ground motion is not strong enough to trigger landslides in the model, with reference to seismic energy source depth  $R_0 = 0$  and assuming 1-s period (1 Hz) seismic waves as the main landslide-triggering factor ( $W_n$  increases with  $M_w$ , varying from ~5 to 50 km for  $M_w$  5–9; Marc et al., 2017), and (2) a “far-field window” centered at the fault rupture with a width ( $W_f$ ) of 4 times of  $W_n$ , that is, ~20–200 km across  $M_w$  5–9, which covers near-field deformations (both footwall subsidence and hanging wall uplift) and a major part of far field deformation. For reference, the widths of modern-day tectonically active mountain belts (e.g., Taiwan) are generally around 50–200 km (Hovius, 1996; Watts, 2001).

### 3.5. Topographic Volume Balance Over Earthquake Cycles

We first consider the seismic volume budget without accounting for the aseismic component. We then introduce aseismic deformation and evaluate how this term affects the seismic volume balance. For seismic volume balance, within a specified spatial window, the erosion term is defined as the volume of earthquake-triggered landslides ( $V_{ls}$ ), whereas the uplift term ( $V_{up}$ ) is determined as the sum of seismic uplift volume ( $V_{up}^{\text{seismic}}$ , resulting from coseismic deformation and postseismic relaxation) and erosion-induced isostatic uplift volume ( $V_{up}^{\text{isostasy}}$ ):

$$V_{up} = V_{up}^{\text{seismic}} + V_{up}^{\text{isostasy}} \quad (9)$$

The seismic volume balance is expressed as the ratio ( $\Omega$ ) between the volume of landslides ( $V_{ls}$ ) versus the uplifted volume ( $V_{up}$ ):

$$\Omega = V_{ls} / (V_{up}^{\text{seismic}} + V_{up}^{\text{isostasy}}) \quad (10)$$

$V_{ls}$  and  $V_{up}^{\text{isostasy}}$  are calculated following the approaches in sections 3.2 and 3.3, and we define their ratio as  $\lambda = V_{up}^{\text{isostasy}}/V_{ls}$ . At regional scales, this ratio is determined by the relative magnitude of the density of the underlying lithosphere versus the asthenosphere (Molnar, 2012). At local scales with given density of the lithosphere and the asthenosphere, this ratio is a function of the parameters determining the extent to which isostasy compensates landslide erosional unloading, specifically lithospheric  $T_e$  and landslide spatial pattern factor  $\beta$ . As noted above, interpretation of our model results using  $\lambda$  is valid only in the context of our modeling framework considering the net effect of multiple earthquake cycles and where 2-D models are suitable (section 2.1); explicit 3-D models would be required to simulate single earthquake events whose rupture length are shorter or of similar length scale as  $T_e$ . With  $\lambda$ , we rewrite the seismic volume balance ratio (equation (10)) as

$$\Omega = V_{ls} / (V_{up}^{\text{seismic}} + \lambda V_{ls}) \quad (11)$$

We next add the aseismic uplift volume ( $V_{up}^{\text{aseismic}}$ ) to the uplift term in equation (8) and define the volume balance over one full earthquake cycle as

$$\Omega^* = V_{ls} / (V_{up}^{\text{seismic}} + V_{up}^{\text{aseismic}} + \lambda V_{ls}) \quad (12)$$

Combining equations (2), (11), and (12), we have

$$\frac{\Omega^*}{\Omega} = \frac{f}{1 + (f-1)\lambda\Omega} \quad (13)$$

$\Omega^*/\Omega$  provides a metric of how the volume balance ratio accounting for aseismic uplift differs from the purely seismic volume balance ratio. Based on equation (13), we explore how  $\Omega^*/\Omega$  varies across  $f$ ,  $\lambda$ , and  $\Omega$ .

### 3.6. Sensitivity Test

To evaluate the relative importance of different model parameters in determining the seismic volume budget, we perform a sensitivity test considering how changes in free parameters affect  $\Omega$ , landslide volume  $V_{ls}$ , seismically uplifted volume  $V_{up}^{\text{seismic}}$ , and the ratio between the volumes of isostatic uplift versus landslides ( $\lambda = V_{up}^{\text{isostasy}}/V_{ls}$ ). The input parameters are  $T_e$ , fault dip  $\theta$ , normalized landslide failure susceptibility  $\delta_{sn}$ , mean rupture depth  $R_0$ , landscape gradient, and landslide spatial decay factor  $\beta$ . We choose the ranges of the

input parameters as observed in real geological settings ( $R_0$ : 2–40 km,  $T_e$ : 2–40 km,  $\log_{10}\delta_{sn}$ : −1~1,  $\theta$ : 10–70°,  $S_{mod}$ : 20–40°,  $1/\beta$ : 0–5; Li et al., 2017; Marc, Hovius, Meunier, Gorum, et al., 2016; Meunier et al., 2007; Watts, 2001). For a series of earthquake magnitudes from  $M_w = 6$  to  $M_w = 9$  and different seismological landslide-triggering factors that give different groups of  $M_h$ ,  $e_5$ ,  $e_6$ , and  $e_7$ , we fix all parameters at their medians, vary one parameter by 10% of the full sampling range at a time, and calculate the corresponding percentage deviation of  $V_{ls}$ ,  $V_{up}^{\text{seismic}}$ ,  $\Omega$ , and  $V_{up}^{\text{isostasy}}/V_{ls}$ . The sensitivity tests are run for both the near-field and the far-field scenarios.

To visualize the model results in multidimensional parameter space, we also present 2-D contour plots calculated using the same ranges for input parameters as used in the sensitivity analysis. We first fix all input parameters at their medians and then vary two parameters over the full range, calculating the difference between the resulting  $\Omega$  and the average of all  $\Omega$  values ( $\bar{\Omega}$ ) as we focus on the relative difference rather than absolute values in this context. We report  $\Omega - \bar{\Omega}$  in 2-D contour plots. To test the sensitivity of  $V_{ls}$  and  $\Omega$  to earthquake depth, we assume that  $V_{up}^{\text{seismic}}$  is constant over varying depth. This assumption may introduce a minor uncertainty (5–10%) to  $V_{up}^{\text{seismic}}$ ; Marc, Hovius, and Meunier (2016) show that coseismic uplift varies by 5–10% at different  $R_0$ , and King et al. (1988) suggest that  $T_e$  exerts the major control on postseismic deformation (i.e.,  $R_0$  plays a minor role). Note that only in this analysis focusing on the relative changes do we make this assumption and vary earthquake depth to calculate  $V_{up}^{\text{seismic}}$ , whereas in other analysis concerning  $V_{up}^{\text{seismic}}$ , we always refer to section 2.1.1 to use fault width and dip angle to estimate depth.

### 3.7. Wenchuan Earthquake Volume Balance Considering Postseismic Effects

In addition to the general consideration of volume budgets for different earthquakes, we apply our approach specifically to the Wenchuan earthquake, where we can combine the model results with empirical observations. The comprehensive studies of earthquake-triggered landslides (e.g., Li et al., 2014; Xu et al., 2014) and seismically induced deformations (e.g., de Michele et al., 2010; Fielding et al., 2013; Huang et al., 2014) following the Wenchuan earthquake make this event an ideal case to study earthquake volume balance. Prior studies (Li et al., 2014; Parker et al., 2011) only considered the volume balance between coseismic uplift and landslide erosion, not taking into account the effects of postseismic relaxation and isostatic responses to erosion. Limited studies (e.g., Huang et al., 2014) have characterized post-Wenchuan deformation using less than two years of geodetic measurements but cannot constrain postseismic deformation over the full earthquake cycle. Note that the seismogenic fault was thought to be fully locked before the Wenchuan earthquake (e.g., Wang et al., 2010); thus, we neglect aseismic slip in this case.

We calculate the volume balance for the Wenchuan event over a full earthquake cycle, combining empirical data on the coseismic uplift and landslide volumes with modeling of the postseismic relaxation and isostatic response. We adopt the landslide map from Li et al. (2014) where landslide volumes were determined using an empirical area-volume scaling relation and coseismic displacement data determined from SAR measurements by Fielding et al. (2013). We also model the coseismic deformation field and earthquake-triggered landslides using the Wenchuan parameters and validate our model results by comparing to field observations. With the coseismic uplift data, we then model the completely relaxed deformation using the approach in section 2.2. We model the flexural-isostatic response to landslide erosional unloading using the approach in section 3.4, assuming complete removal of landslide debris between earthquake cycles. For the effective elastic thickness  $T_e$ , we consider values of 10, 20, 30, and 40 km, recognizing that estimates of  $T_e$  in the Wenchuan region vary broadly from ~7 to 40 km (Densmore et al., 2012, and references therein).

To better understand how earthquakes drive topographic development of the eastern Tibetan Mountains where the Wenchuan earthquake occurred, we then consider the volume balance over multiple earthquake cycles for the Wenchuan region. We calculate the volume balance ratio for each earthquake magnitude using the parameters constrained from the Wenchuan data and estimate the probability distribution of  $\Omega$  over multiple earthquake cycles to evaluate the net topographic effect of seismicity in this region.

## 4. Results

### 4.1. Patterns of Seismically Induced Deformations

Over one full earthquake cycle, different processes contribute to producing distinct topographic structures. Coseismic deformation creates focused uplift in a narrow zone above the fault plane, with far-field

subsidence on the hanging wall, and a combination of near-field subsidence and far-field bulging on the footwall (Figure 4a). Postseismic relaxation distributes the localized, coseismic deformation to far-field areas, reducing the near-field uplift and enhancing the hanging wall's far-field uplift and the footwall's subsidence (Figures 4a–4c). These deformation patterns depend in part on dip angle of the seismogenic fault (Figures 4a–4c). Notably, the modeled seismic deformation produces similar topographic features as simple back slip models (e.g., Savage, 1983), a propagator matrix-based analytical model (King et al., 1988; Thatcher & Rundle, 1984), and a viscoelastic finite element model (Simpson, 2015). Earthquake-triggered landslide erosion mainly focuses in a narrow zone and rapidly decays in the far field (Figure 4d). Flexural-isostatic compensation to erosional unloading is more widely distributed as compared to landsliding, featuring a bulge in the near field and depressions in the far field (Figures 4d and 4e).

#### 4.2. Variations of the Seismically Induced Volumes Over Input Parameters

As shown in equation (10), the earthquake volume balance ratio  $\Omega$  is determined by the landslide volume  $V_{ls}$ , the seismic uplift volume  $V_{up}^{seismic}$  as induced by coseismic and postseismic deformation, and  $\lambda$ , the ratio between the isostatically uplifted volume  $V_{up}^{isostasy}$  and  $V_{ls}$ . Here we explore the variations of  $V_{ls}$ ,  $V_{up}^{seismic}$ , and  $\lambda$  across the studied ranges of the input parameters as reported in section 3.6, with earthquake magnitude varying from  $M_w = 6$  to  $M_w = 9$ .

$V_{up}^{seismic}$  varies as a function of earthquake magnitude  $M_w$ , lithospheric  $T_e$ , and fault dip  $\theta$ . Across the range of these parameters,  $V_{up}^{seismic}$  has the most significant variation as a function of  $M_w$  (~1,000 times with  $M_w \sim 6\text{--}9$ ), relatively moderate variation over  $T_e$  (~10 times for  $T_e$  from 2 to 40 km), and limited change over  $\theta$  (~1–3 times for  $\theta$  from 30 to 60°), as illustrated by the color contours in Figures 5a and 5b. The effects of  $T_e$  and  $M_w$  are similar for near-field and far-field scenarios (Figures 5a and 5b). However,  $V_{up}^{seismic}$  shows opposite trends as a function  $\theta$  in the far-field scenario (Figure 5b), which is caused by the fact that the far-field window includes both local uplift and subsidence which increase together as  $\theta$  grows, but the subsidence term increases faster, offsetting the uplift term and leading to a smaller  $V_{up}^{seismic}$ .

$V_{ls}$  is similar in the near-field window and the far-field window (section 3.5), so we just consider the total volume of  $V_{ls}$ . Mean rupture depth  $R_0$  is a major control on  $V_{ls}$ , causing changes in  $V_{ls}$  (up to 10,000 times across the selected range of  $R_0$ ) comparable to or even exceeding changes over  $M_w$  (Figure 5c). The  $V_{ls}\text{-}M_w$  relations differ depending on the assumed landslide-triggering factor, with the maximum  $V_{ls}$  corresponding to 4-s period (0.25 Hz) S waves (Figure 5e). Notably, for a given earthquake magnitude, the variation of  $V_{ls}$  calculated assuming different landslide-triggering factors is comparable to the entire range of  $V_{ls}$  across the studied earthquake magnitudes, emphasizing the importance of landslide-triggering mechanisms in  $V_{ls}$  and the earthquake volume balance (Figure 5e).  $V_{ls}$  has a moderate dependence on landscape failure susceptibility and steepness, showing ~100 times and ~10 times variations across their studied ranges, respectively (Figures 5d and 5f).

For isostatic response, in the far-field scenario,  $\lambda$  is a constant determined by the ratio of the density of lithosphere versus that of the asthenosphere (Molnar, 2012; Molnar & England, 1990). In the near-field scenario,  $\lambda$  is in theory controlled by the lithospheric rigidity and the spatial pattern of landslides (Densmore et al., 2012). The near-field  $\lambda$  has a strong dependence on  $T_e$  and a relatively weak dependence on the spatial pattern factor of landslides,  $\beta$ , and is insensitive to changes in  $M_w$  (Figures 5g and 5h). The decreasing trend of near-field  $\lambda$  with  $T_e$  is expected because higher  $T_e$  means higher lithospheric rigidity and causes more distributed isostatic uplift over broader areas.

The sensitivity analysis complements the above calculations and allows us to evaluate the relative importance of different parameters in the earthquake volume balance (Figure 6). The signs of the calculated sensitivities also indicate whether increasing a parameter would increase (positive) or decrease (negative) the uplift and landslide volumes and the related volumetric ratios. We have considered a series of earthquake magnitudes, different landslide-triggering factors that are representative of the observed  $\Omega\text{-}M_w$  patterns (discussed later in section 5.1 and in Figure 9), and the effect of spatial windows. In the near-field scenario, the volume balance ratio ( $\Omega$ ) is highly sensitive to the landslide volume-related parameters including  $R_0$ ,  $\delta_{sn}$ ,  $S_{mod}$ , moderately sensitive to  $T_e$  and  $\theta$ , and almost insensitive to landslide spatial pattern factor  $\beta$  (Figure 6). In most cases,  $\Omega$  is most sensitive to mean rupture depth  $R_0$ . Exceptional cases appear where landslides are triggered by waves of 4-s period (0.25-Hz frequency) and  $M_w \geq 8$ , where  $\Omega$  and  $V_{ls}$  is most sensitive

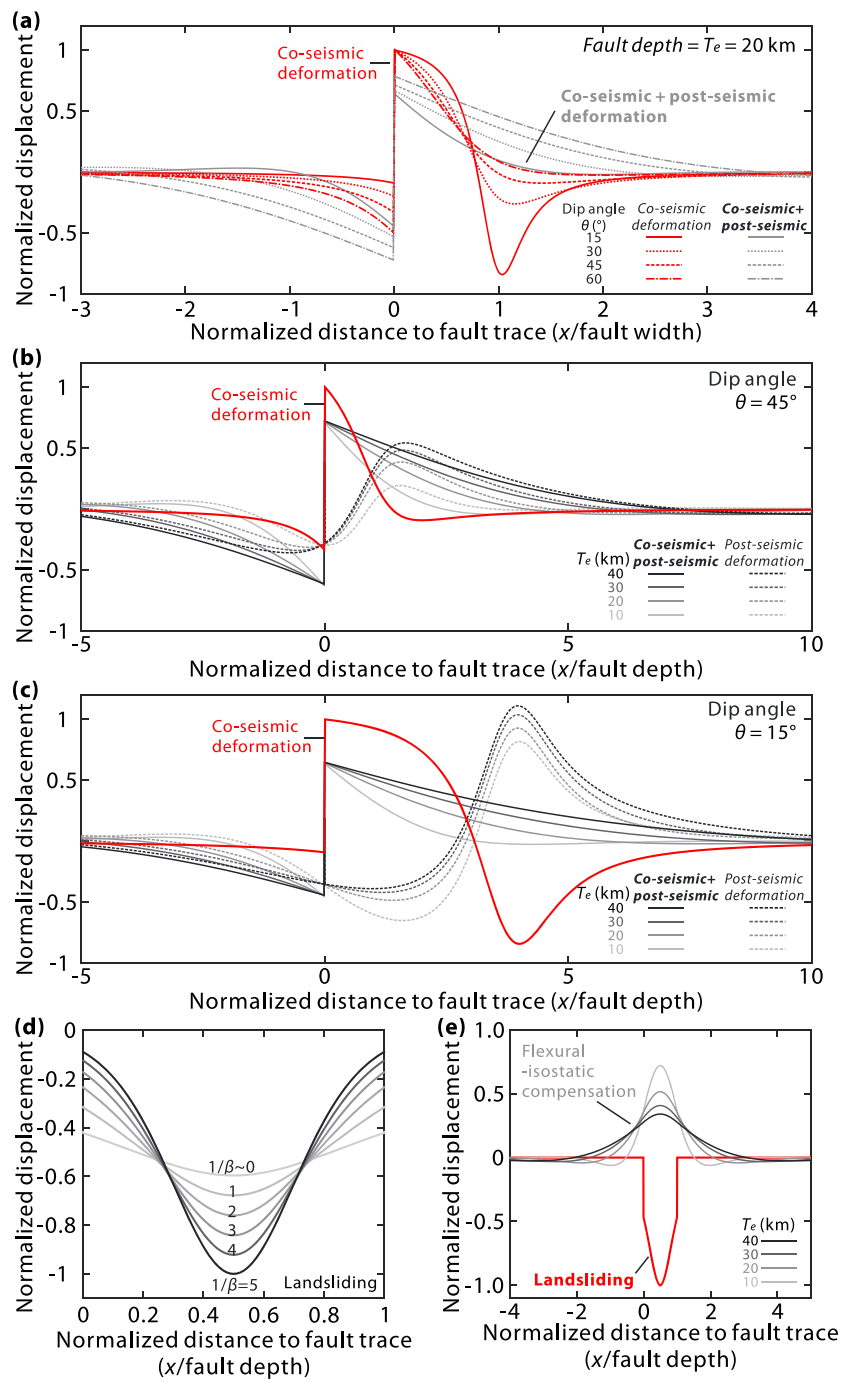


**Figure 4.** Spatial patterns of seismically induced deformations over full earthquake cycles and variations over controlling parameters. (a) Normalized vertical displacements of coseismic deformation (red lines) and the combined coseismic and postseismic deformation (gray curves) with varying fault dip and  $T_e$  values versus distance to fault trace normalized by fault width. (b) Normalized vertical displacements caused by coseismic deformation (red lines), postseismic deformation (dashed gray curves), and the combined coseismic and postseismic deformation (solid gray curves) with a fault dip  $\theta$  of  $45^\circ$  and varying  $T_e$  values versus distance to fault trace normalized by fault depth, and the same type of results for a fault dip  $\theta$  of  $15^\circ$  are plotted in (c). (d) Normalized vertical displacement of landslide erosion as a function of landslide spatial pattern factor  $\beta$ . (e) Normalized vertical displacement of flexural-isostatic compensation to landslide erosion ( $\beta = 1$ ) over changing  $T_e$ . In (d) and (e), the modeled landslides are set to occur only on the hanging wall ( $x/\text{fault depth} > 0$ ). Note the different horizontal scales in the  $x$  axes, and the  $x$  axis in (a) is normalized to fault width, whereas for other panels the  $x$  axis is normalized to fault depth (fault depth = fault width  $\times \sin\theta$ ). Here we consider earthquake rupture depth is equal to fault depth and  $T_e$ .

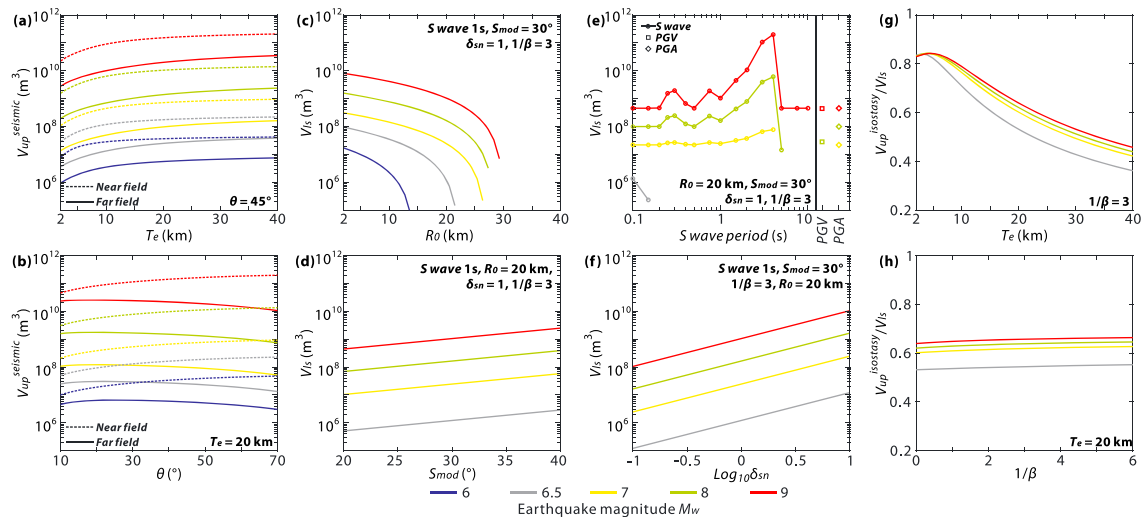


**Figure 5.** Seismically induced volumes and the isostatic ratio as a function of input parameters and assumptions about landslide-triggering factors, including  $V_{up}^{\text{seismic}}$  versus (a)  $T_e$  and (b)  $\theta$ ;  $V_{ls}$  versus (c)  $R_0$ , and (d)  $S_{mod}$ , (e) assumed landslide-triggering factor including seismic waves of different frequencies, PGV, and PGA; and near-field isostasy ratio versus (g)  $T_e$ , (f)  $\delta_{sn}$ , and (h)  $1/\beta$ .  $V_{up}^{\text{seismic}}$  considers both far-field and near-field scenarios, that is, the solid and dashed lines in (a) and (b), respectively. Adopted values of relevant model parameters are reported in each panel.

to failure susceptibility and less sensitive to  $R_0$ .  $V_{up}^{\text{seismic}}$  shows low sensitivity to  $\theta$  and  $T_e$ . The near-field isostasy ratio  $\lambda$  responds weakly to changes in  $T_e$ , with no obvious responses to changes in other parameters. Considering the meaning of the signs, the sensitivity analysis predicts that erosive earthquakes should occur in cases with shallower  $R_0$ , thinner  $T_e$ , higher failure susceptibility, lower dip,

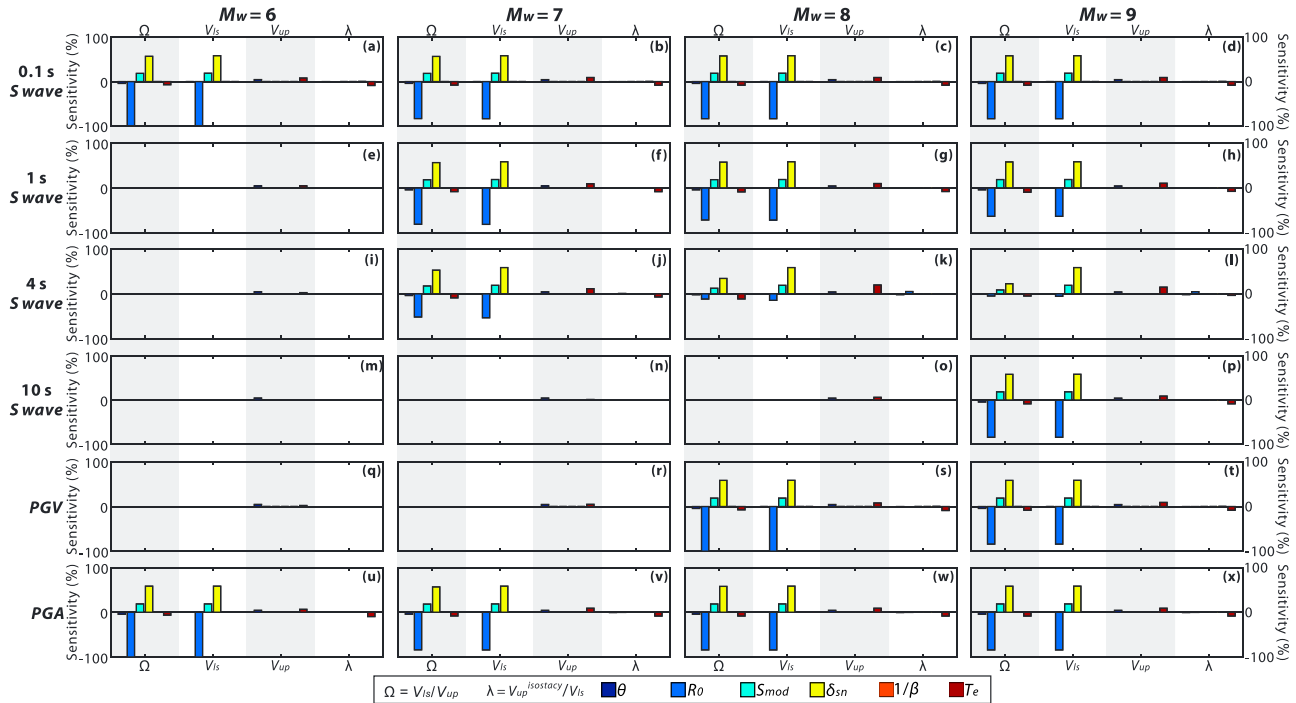


**Figure 6.** Sensitivity analysis of earthquake volume balance ratio  $\Omega$ ,  $V_{ls}$ ,  $V_{up}$ , and  $\lambda$  to changes in the studied parameters over different earthquake magnitudes and seismological factors responsible for triggering landslides (e.g., S waves of different periods, PGV and PGA) for near-field scenario. Panels showing blank results (e.g., (e), (i), (m), and (q)) mean no landslides are triggered with the given conditions. The signs indicate the changes of the ratios and uplift volumes when increasing a parameter: positive means increase and negative means decrease.

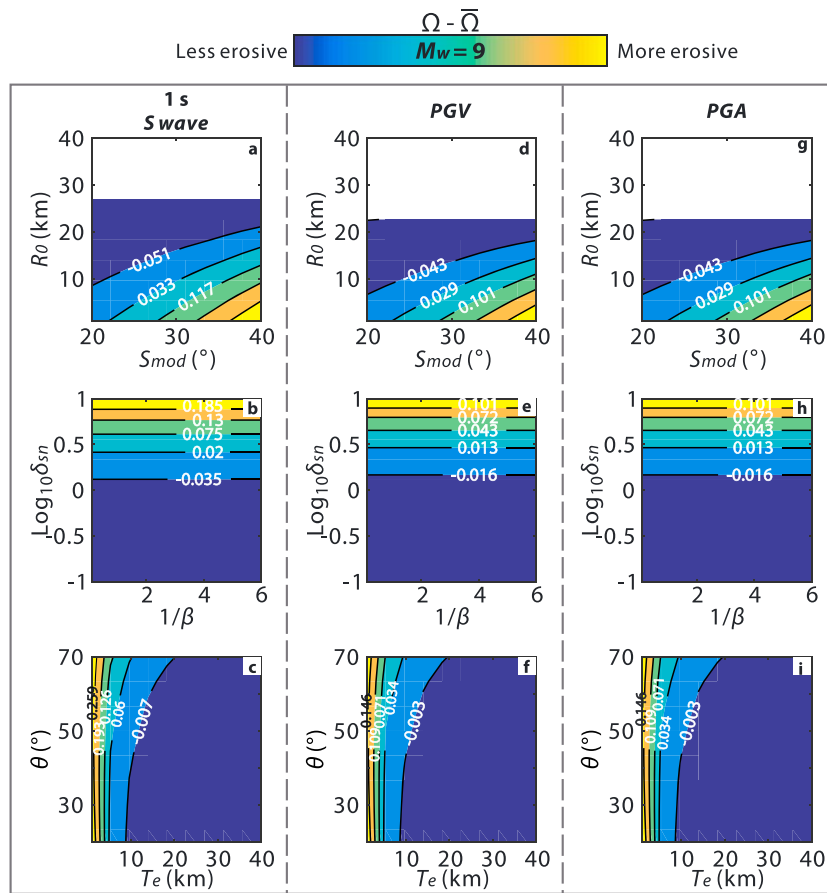


**Figure 7.** Contour plots of the relative earthquake volume balance ratio, defined as the difference between the earthquake volume balance ratio  $\Omega$  and the average volume balance ratio  $\bar{\Omega}$  over the sampling space. We consider  $M_w = 9$  here and a range of representative seismological factors (S wave of 1-s period, PGV and PGA) responsible for triggering landslides in a far-field scenario. Blank areas (in (a), (d), and (g)) represent no landslides being triggered for the given conditions. The values of the input parameters and sampling ranges are detailed in section 3.6. Please see more contour plots for various earthquake magnitudes and a more complete set of landslide-triggering factors in the Appendix A.

and steeper  $S_{mod}$ , and would not be influenced much by the spatial pattern of landslides. In far-field scenarios, most findings are consistent with the near-field cases, except that the isostasy ratio has almost no sensitivity to  $T_e$  and other parameters, as in this case  $\lambda$  is determined by the density difference between the lithosphere and asthenosphere. Also, in the far-field case, higher fault dip would lead to lower  $V_{up}^{seismic}$  and consequently higher  $\Omega$ , opposite to the near field, as also shown in Figure 5b.

The contour plots also help to illustrate how  $\Omega$  varies in the multidimensional parameter space, complementing the above sensitivity analysis (Figures 7 and A1, A2, A3, A4). In these plots, we report  $\Omega - \bar{\Omega}$ , the changes of  $\Omega$  relative to the average value of  $\Omega$  in the sampling parameter space (see section 3.6), and we show results for the far-field scenario. The contour plots show that, in general, the earthquake volume balance ratio is sensitive to  $R_0$ ,  $S_{mod}$ , and  $\delta_{sn}$  and relatively insensitive to  $\theta$  and  $\beta$ . Sensitivity to  $T_e$  decreases as the absolute value of  $T_e$  increases. Similar to the sensitivity analysis, we also note that the 4-s period represents an extremely erosive scenario (e.g., for  $M_w \geq 7$ ,  $\Omega \sim 1$ , and  $V_{ls}/V_{up}^{seismic} \sim 5$ ; Figures 7 and A2, A3, A4) where earthquakes at deeper depth (>20 km) can still trigger landslides (e.g., Figure A4g) and  $\Omega$  becomes insensitive to increases in  $V_{ls}$  (e.g., Figure A4h) because the uplift term is dominated by landslide erosion-induced isostasy such that  $\Omega$  is close to the ratio of  $V_{ls}/V_{up}^{isostacy}$ , which is relatively stable in far-field scenarios. However,  $\Omega$  is still sensitive to changes in  $T_e$ ,  $\theta$ , and thus  $V_{up}^{seismic}$ , when  $V_{ls}$ -controlling parameters are fixed (e.g., Figure A4i). The near-field scenario shows similar trends as the far-field results, except for  $\theta$  which has the opposite effect (Figure 5b).

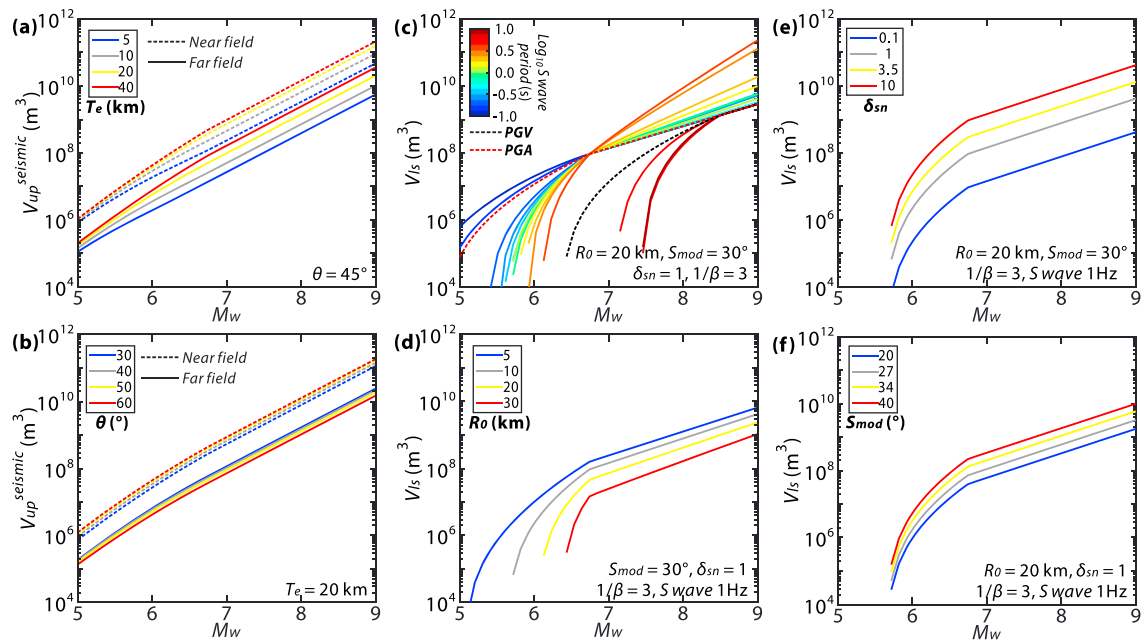


**Figure 8.** Variations of seismically induced uplift and landslide volumes across earthquake magnitudes over different parameters and possible seismological landslide-triggering factors. (a)  $V_{up}^{seismic}$  versus  $M_w$  under changing  $T_e$  (colored) in near-field (dashed lines) and far-field (solid lines) scenarios. (b)  $V_{up}^{seismic}$  versus  $M_w$  under changing  $\theta$  (colored) in near-field (dashed lines) and far-field (solid lines) scenarios. (c)  $V_{ls}$  versus  $M_w$  under changing seismological factors responsible for triggering landslides. (d)  $V_{ls}$  versus  $M_w$  under changing seismological factors responsible for triggering landslides. (e)  $V_{ls}$  versus  $M_w$  under changing landscape failure susceptibility. (f)  $V_{ls}$  versus  $M_w$  under changing landscape steepness. Adopted values of relevant model parameters are reported in each panel.

Overall, the above analysis demonstrates that in most cases, earthquake magnitude is the dominant control on the volume of both the uplifted topography and landslides, consistent with attention on this parameter in prior studies (Li et al., 2014; Marc, Hovius, & Meunier, 2016). For a given earthquake magnitude, seismological landslide-triggering factors, mean rupture depth, and lithospheric effective elastic thickness can modulate the earthquake volume budget.

## 5. What Is the Role of Earthquake Magnitude?

### 5.1. Volume Balance Across Earthquake Magnitudes ( $\Omega$ -earthquake magnitude relations)

In this section, we revisit the problem of earthquake volume balance over varying earthquake magnitudes, previously considered by Li et al. (2014) and Marc, Hovius, and Meunier (2016). Here we consider how post-seismic processes influence this analysis, and how conclusions are sensitive to assumptions about the seismic properties responsible for triggering of landslides. As fault size and the generated earthquake magnitudes vary both spatially and temporally, the  $\Omega$ - $M_w$  pattern provides key information about the spatiotemporal variability in the erosivity of earthquakes.

Across the selected ranges of  $T_e$  and  $\theta$ ,  $\log_{10}(V_{up}^{seismic})$  scales mostly linearly with  $M_w$  (Figures 8a and 8b); the gentle curvature is an artifact caused by integrating volumes within defined spatial windows. The modeled  $V_{ls}$ - $M_w$  relations feature a kink corresponding to the seismic hinge magnitude beyond which ground motion saturates (Figures 8c–8f). Assumptions about landslide-triggering factors play a first-order role in determining the  $V_{ls}$ - $M_w$  relations, determining not only where the “kink” (hinge magnitude) is but also the curvature in the relationships and the absolute values of  $V_{ls}$  (Figure 8c). For a given landslide-triggering factor, mean rupture depth  $R_0$  does not influence the location of the kink and the  $V_{ls}$ - $M_w$  curvature beyond the hinge magnitude, but impacts the absolute values of  $V_{ls}$  and the curvature when  $M_w$  is smaller than the hinge magnitude (Figure 8d). In contrast, landscape failure susceptibility and steepness only affect the absolute values of  $V_{ls}$  but not the patterns of the  $V_{ls}$ - $M_w$  curves (Figures 8e and 8f). These differences ultimately control the balance between uplift and landslide erosion for a single event (Figures 8a–8d).

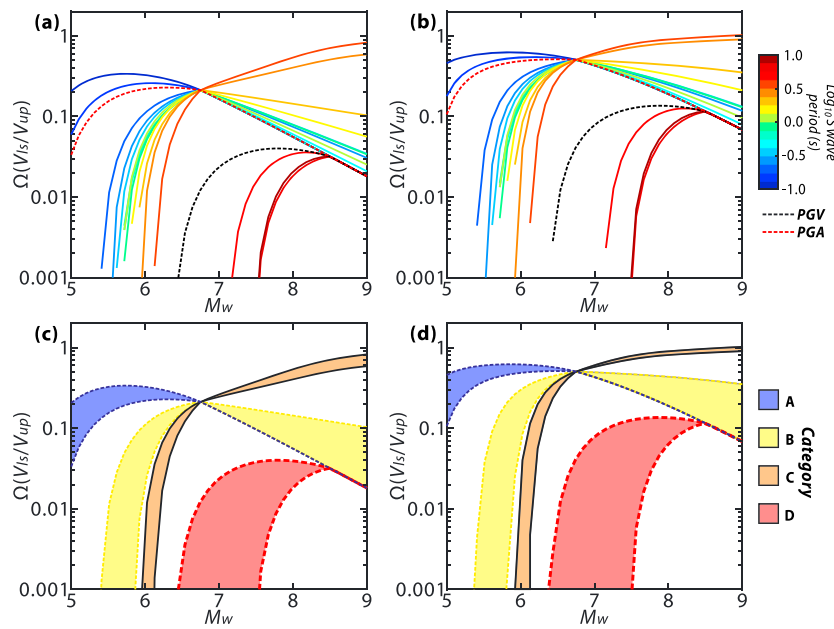


**Figure 9.** Earthquake volume balance ratio across earthquake magnitudes over possible seismological factors responsible for triggering landslides, accounting for (a) near-field and (b) far-field scenarios. (c and d) The representative patterns (color-labeled as categories A–D) as plotted in (a) and (b), respectively. The related parameters are set at their medians of the ranges reported in section 2.7. The input parameters are  $\theta = 45^\circ$ ,  $T_e = 20$  km,  $R_0 = 10$  km,  $S_{mod} = 30^\circ$ ,  $1/\beta = 1$ , and  $\delta_{sn} = 1$ .

Since the seismic triggering factor exerts a first-order control on the  $V_{ls}$ - $M_w$  relationship, we calculate volume balance ( $\Omega$ ; the ratio of  $V_{ls}$  to  $V_{up}^{\text{seismic}}$ ) across earthquake magnitudes considering different assumed landslide-triggering factors (Figure 9a for near-field and Figure 9b for far-field scenarios). We report the results for fixed values of other input parameters ( $\theta = 45^\circ$ ,  $T_e = 20$  km,  $R_0 = 10$  km,  $S_{mod} = 30^\circ$ ,  $1/\beta = 1$ , and  $\delta_{sn} = 1$ ) and note that changing these parameter values will change the absolute values of volume balance ratio, as detailed in the sensitivity analysis in section 4.2 and Figure 6, but the overall trends in the  $\Omega$ - $M_w$  relationships should remain similar. In general, we find four types of  $\Omega$ - $M_w$  relationships: (1) “hump” curves featured by peak  $\Omega$  around  $M_w$  5–6 (category A in Figures 9c and 9d, for waves with periods of 0.1–0.2 s and PGA), (2) hump curves with peak  $\Omega$  around  $M_w$  6.7 (category B in Figures 9c and 9d, for waves with periods of 0.2–2 s), (3) hump curves with peak  $\Omega$  around  $M_w$  8–9 (category D in Figures 9c and 9d, for S waves with periods of 5–10 s and PGV), and (4) curves which increase monotonically with  $M_w$  featured by kinks at  $M_w$  6.7 (category C in Figures 9c and 9d, for S waves with periods of 3–4 s). The  $\Omega$ - $M_w$  pattern of type (2) is similar to that reported in Marc, Hovius, and Meunier (2016), where 1-Hz S waves are the major trigger of landslides, such that intermediate-magnitude earthquakes are most erosive and earthquakes of smaller or greater magnitudes are more constructive. The  $\Omega$ - $M_w$  pattern of type (4) is similar to that reported in Li et al. (2014), in which earthquakes of higher magnitudes tend to be more erosive. As noted above, changes in other parameters or the spatial window will change the absolute values of  $\Omega$  but will not change the general patterns of the  $\Omega$ - $M_w$  relationships. We note that seismological landslide-triggering factors exert a major control of the patterns of  $\Omega$ - $M_w$  relationships but have much less influence on the previous sensitivity analysis and contour-based illustration of  $\Omega$  across the multiple-dimensional parameter space (e.g., Figures 6 and 7). Postseismic processes, while important in determining the magnitude and spatial distribution of deformation, do little to affect the shape of the relationship between the volume balance and earthquake magnitude. Our results thus highlight the role of the seismological landslide-triggering factors in setting the relative erosivity of earthquakes as fault systems develop (e.g., Ben-Zion, 2008; Hillers et al., 2007; Milliner et al., 2016; Wesnousky, 1988, 1994). Since much remains unknown about which seismic factors are most important in landslide triggering and how this sensitivity varies, we suggest that better defining the seismic factors responsible for triggering landslides is needed in future studies.

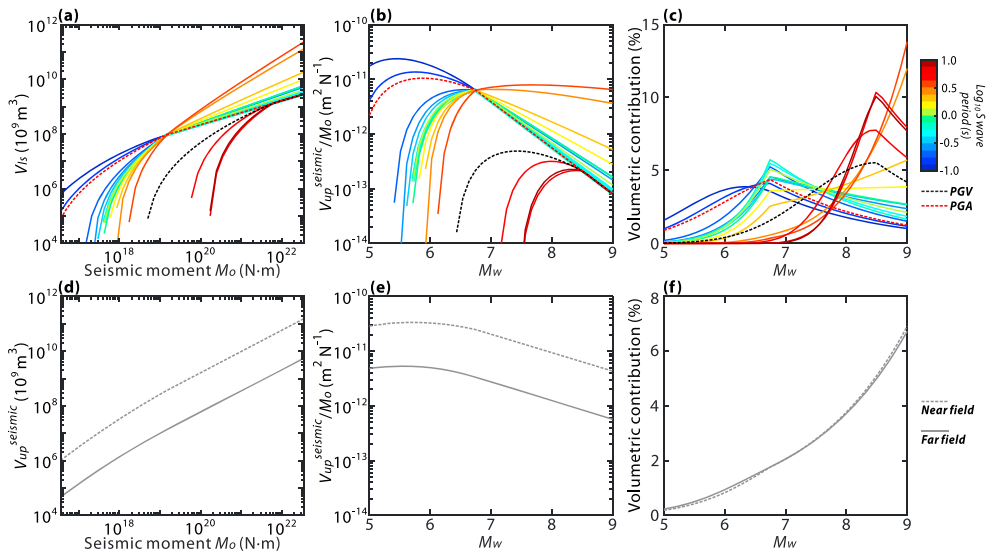


**Figure 10.** Seismically induced uplift and landslide volumes versus seismic moment release and earthquake magnitude. (a)  $V_{ls}$  versus  $M_o$  under changing seismological factors responsible for triggering landslides. (b)  $V_{ls}/M_o$  versus  $M_w$  under changing seismological factors responsible for triggering landslides. (c) Contribution to the total landslide volume over multiple earthquake cycles versus  $M_w$ , considering changing seismological factors responsible for triggering landslides. For  $V_{ls}$  calculations, the input parameters are  $R_0 = 1\text{--}40 \text{ km}$ ,  $S_{mod} = 30^\circ$ ,  $\delta_{snl} = 1$ , and  $1/\beta = 1$ . (d)  $V_{up}^{\text{seismic}}$  versus  $M_o$  for near-field (dashed curve) and far-field (solid curve) scenarios. (e)  $V_{up}^{\text{seismic}}/M_o$  versus  $M_w$  for near-field (dashed curve) and far-field (solid curve) scenarios. (f) Contribution to the total seismic uplift volume over multiple earthquake cycles versus  $M_w$ , considering near-field (dashed curve) and far-field (solid curve) cases. For  $V_{up}^{\text{seismic}}$  calculations, we choose  $\theta = 45^\circ$ ,  $T_e = 20 \text{ km}$ , and determine rupture dimensions using  $M_w$ -based scaling relations and earthquake depth combining fault width and dip angle.

## 5.2. Efficiency of Eroding and Uplifting Topography Depends on Earthquake Magnitude

Earthquakes make use of seismic energy release to uplift topography, thus increasing gravitational potential. Earthquakes also use seismic energy to overcome cohesion and friction resistance, triggering landslides. In these respects, the processes by which earthquakes build and erode topography can be conceptualized as energy conversion (Muenchow et al., 2012; Wolman & Miller, 1960), and we can think of earthquakes as using seismic energy to drive landscape change. For different earthquake magnitudes, the ratio between seismically eroded or uplifted volume versus seismic moment release (i.e., the amount of landscape change induced per unit energy), represents the efficiency of earthquakes in driving topographic change. With this concept in mind, we calculate the seismic moment  $M_o$  (N · m) from  $M_w$  using equation (14) (Hanks & Kanamori, 1979):

$$\log_{10} M_o = 1.5M_w + 9.05 \quad (14)$$

and we consider  $V_{up}^{\text{seismic}}$  and  $V_{ls}$  as a function of  $M_o$ , respectively (Figure 10).

Considering landslide erosion, the  $M_o$ - $V_{ls}$  relations tend to have shallower slopes at higher  $M_o$  (Figure 10a). The  $M_o$ -normalized landslide volume shows rapid increases at lower magnitude, peaks near the corresponding hinge magnitude, and gradually decays toward higher magnitudes (Figure 10b). This pattern is independent of the assumed landslide-triggering factor, and the decaying trends toward higher magnitudes are consistent with the saturation effect on ground motion (Boore & Atkinson, 2008). The modeled  $V_{ls}/M_o$ - $M_w$  relations suggest that for the same seismological and topographic conditions and within the range of earthquake magnitudes that trigger landslides ( $M_w > 5$  in this context), smaller-size events are more efficient in generating landsliding and eroding topography as compared to larger-size events. Notably, this finding updates the understanding of Keefer (1994) which showed that  $V_{ls}$  scales linearly with  $M_o$ , suggesting a uniform efficiency in eroding topography across earthquake magnitudes, with a more comprehensive consideration of the seismological factors triggering landslides.

For the uplifted volume,  $V_{\text{up}}^{\text{isostasy}}$  scales linearly with  $V_{ls}$  under given  $T_e$  and thus is expected to display the same behavior as  $V_{ls}$  (Figures 10a and 10b). Similar to  $V_{ls}$ , the  $V_{\text{up}}^{\text{seismic}}-M_o$  relations also have shallower slopes at higher  $M_o$  (Figure 10d), and the  $M_o$ -normalized seismically uplifted volume decreases toward higher magnitude (Figure 10e), suggesting lower efficiency of high-magnitude events. This finding is actually expected when considering the scaling relations between fault dimensions, earthquake magnitude, and seismic moment. By definition, seismic moment is the product of shear modulus  $\mu$ , fault displacement  $D$ , and fault rupture area  $A$ :

$$M_o = \mu \times A \times D \quad (15)$$

and fault rupture area  $A$  is the product of fault rupture length  $L$  and fault width  $W$  assuming a rectangular rupture surface:

$$A = W \times L \quad (16)$$

Fault rupture length  $L$ , fault width  $W$ , and fault displacement  $D$  all scale with  $M_o$  (Leonard, 2010). As derived in Li et al. (2014), the coseismically uplifted volume is proportional to product  $A \times D$  or  $W \times L \times D$ , and thus scales linearly with seismic moment  $M_o$ , indicating a power law exponent of one and uniform efficiency across earthquake magnitudes. Whereas fault width  $W$  dictates the horizontal wavelength of the coseismically uplifted topography (Li et al., 2014), the effect of postseismic relaxation depends heavily on  $T_e$  that is independent of  $M_o$ . Thus, over a full earthquake cycle, the dependence of  $V_{\text{up}}^{\text{seismic}}$  on  $W$  and  $M_o$  is reduced, leading to a power law exponent smaller than 1, that is, a decreasing trend in the  $V_{\text{up}}^{\text{seismic}}/M_o$ - $M_o$  relation. Due to the limitations of our 2-D calculation, we cannot directly evaluate the dependence on fault length, which likely has more profound influence for single earthquakes with shorter rupture length and requires further examination in 3-D models.

When considering how seismic energy release drives topographic change, larger earthquakes are less efficient both in terms of landslide erosion and uplift, compared to their smaller relatives. This suggests that as fault systems mature and are capable of accommodating higher  $M_w$  events, it is possible that the efficiency of both inducing landslide erosion and producing topography may decrease. At the same time, growing fault zones can promote structure complexities and local deformation features that could limit high-magnitude events (e.g., Wesnousky, 1994), potentially complicating how they release seismic energy and cause topographic change.

Normalizing volumes by seismic moment helps in evaluating the efficiency of earthquakes of different magnitudes, both in terms of landslide erosion and seismically induced uplift. However, over multiple earthquake cycles, earthquake recurrence time depends on earthquake magnitude. We take into account the  $M_w$ -earthquake recurrence time relation in order to evaluate how earthquakes of different magnitudes contribute to the cumulative topographic changes over longer time scales of multiple earthquakes. Taking the same approach as in section 2.1, we model earthquake sequences over multiple seismic cycles using a Gutenberg-Richter  $M_w$ -frequency distribution. We consider a common fault setting where  $\theta = 45^\circ$ ,  $T_e = 20$  km,  $S_{\text{mod}} = 30^\circ$ ,  $\delta_{sn} = 1$ , and  $1/\beta = 1$ , and allow earthquake depth and magnitude to vary. We then calculate the total seismically eroded landslide volume within each earthquake magnitude bin ( $\Delta M_w = 0.1$ ), as the product of the recurrence time of the earthquakes in the magnitude bin and the corresponding  $V_{ls}$ , respectively. We perform this calculation for a broad range of  $R_0$  (1–40 km) and integrate  $V_{ls}$  over  $R_0$  for each earthquake magnitude bin. We then quantify the contribution from each earthquake magnitude bin to the total volume budget over multiple earthquake cycles. Similarly, we calculate the contribution to the total seismic uplift from earthquakes of varying magnitudes, but we set earthquake depth equivalent to the product of fault width and  $\sin(\theta)$ , although we expect that varying depth would cause limited influence to  $V_{\text{up}}^{\text{seismic}}$  (e.g., Marc, Hovius, & Meunier, 2016; section 3.6).

As shown in Figure 10c, medium-to-high-magnitude earthquakes are the most significant contributors to landslide erosion, and the magnitudes of maxima volumetric contribution correspond to the hinge magnitude beyond which ground motion saturates (Figure 9). This finding further emphasizes the importance of landslide-triggering mechanisms in understanding the volume budget of earthquakes.

As shown in Figure 10f, high-magnitude earthquakes, though occurring less frequently, contribute most to the total uplifted volume than the more frequently occurring, small-medium-magnitude earthquakes.

## 6. Postseismic Processes and Wavelengths of Deformations

### 6.1. Effect of Postseismic Processes in Seismic Mountain Building

Postseismic processes represent the rheological response of the lithosphere-asthenosphere system to surface changes induced coseismically and over the earthquake cycle, but the effect of postseismic processes has not been considered in previous models of earthquake volume balance (Li et al., 2014; Marc, Hovius, & Meunier, 2016). For a given landslide volume model and landslide-triggering factor, postseismic processes do not fundamentally change the relative volume balance across  $M_w$ , that is, the pattern in Figures 6 and 7, as compared to prior coseismic studies (Li et al., 2014; Marc, Hovius, & Meunier, 2016). However, postseismic processes could cause large variations in the absolute values of uplift volumes, and thus affect whether earthquakes are net constructive or erosive. Specifically, postseismic relaxation enhances hanging wall uplift and footwall subsidence, and isostasy causes distributed uplift (Figure 4). The net topographic effects of these processes and their volume budget vary in different seismotectonic and landscape settings, as evidenced by changes of  $V_{up}^{seismic}$  and  $\lambda$  versus the studied seismotectonic and landscape parameters (Figure 5). Isostasy offsets a major part of landsliding (Molnar, 2012) but does not entirely compensate for the erosional losses, such that some earthquakes that trigger landslides of large enough volumes (e.g., 10 times of  $V_{up}^{seismic}$ ) can still be net erosive over the time scale of earthquake cycles, although such highly erosive events have been rarely observed (e.g., considering landslide volume compilation in Marc, Hovius, Meunier, Gorum, et al. (2016)).

Notably, across the assumed landslide-triggering mechanisms and the selected range of the model parameters, far-field  $\Omega$  is systematically higher than near-field  $\Omega$  (Figure 9). Since  $V_{ls}$  remains similar in both near-field and far-field cases, this difference is caused by the fact that far-field  $V_{up}$  is smaller than near-field  $V_{up}$  with the studied range of the parameters. The difference in  $V_{up}$  for near versus far field emerges because  $V_{up}$  is composed of the seismically uplifted volume  $V_{up}^{seismic}$  and the isostatically uplifted volume  $V_{up}^{isostasy}$ , and  $V_{up}^{seismic}$  is the sum of local uplift and subsidence. When expanding the spatial window, there is a trade-off between isostatic uplift versus seismically induced subsidence. In the near-field scenario, for given  $T_e$  and landslide pattern,  $V_{up}^{isostasy}$  is minimal because the majority of the isostatic uplift is distributed in the far field, but  $V_{up}^{seismic}$  is maximal as most subsidence lies outside this window. Vice versa, in the far-field window,  $V_{up}^{isostasy}$  and seismically induced subsidence both increase, but seismic subsidence outpaces isostatic uplift, leading to the reduction of the total  $V_{up}$ , and consequently a higher value of  $\Omega$ , as shown in Figure 6. Such effects are mainly observed in cases where  $V_{ls}$  is smaller or comparable to  $V_{up}^{seismic}$ . For extremely erosive events when earthquakes trigger large enough volumes of landslides (e.g., 10–100 times of  $V_{up}^{seismic}$ ), it is possible that  $V_{up}^{isostasy}$  outweighs seismically induced subsidence, leading to a higher  $V_{up}$  in the far-field window. However, we expect that such events rarely if ever occur in nature, such that the importance of isostasy is secondary to the counteraction of uplift by subsidence (e.g., Barlow et al., 2015).

Overall, we conclude that postseismic effects exert a secondary influence on the relative patterns of  $M_w$ -earthquake volume balance relation, but can meaningfully affect the spatial patterns.

### 6.2. Wavelength of Seismically Produced Topography and Tectonic Implications

The spatial patterns of seismic and postseismic deformations may contribute to the morphology of the tectonic features observed today. Earthquake-triggered landslides are concentrated in the near field but the corresponding isostatic responses broaden the region of deformation relative to coseismic effects alone (Figure 4). Postseismic relaxation also distributes coseismic uplift and subsidence to the far field. Thus, we expect erosion to be focused near range-bounding faults (Li et al., 2017), while uplift and subsidence extend over wide areas. This pattern of concentrated erosion and distributed uplift and subsidence is consistent with the structure of a range-basin system where erosion is focused along mountain fronts and uplift and subsidence are distributed broadly, demonstrating that earthquakes can produce such tectonic features. Another interesting observation is that the wavelength of seismically created topography scales with  $M_w$  and  $T_e$  (Figure 11). This finding suggests that in landscapes controlled by seismogenic fault systems

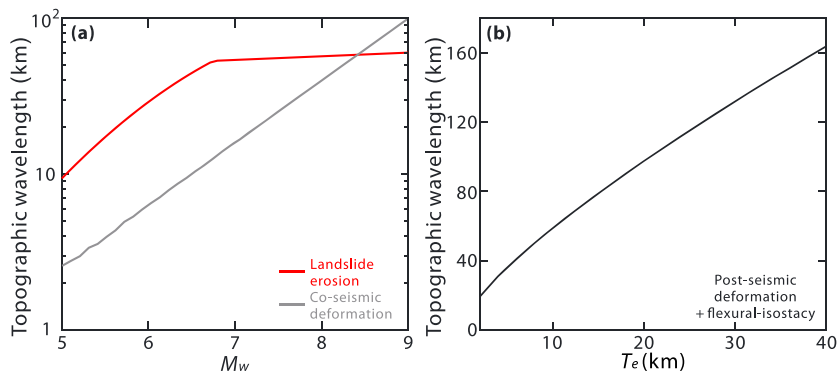


**Figure 11.** Wavelength of seismically produced topography versus (a)  $M_w$  and (b)  $T_e$ , considering topographic wavelength caused by (a) coseismic deformation (gray curve, wavelength defined as the horizontal range within 20% of maximum deformation), landslide erosion (red curve, wavelength defined as the horizontal width of the full landslide erosion zone, using the relation from Marc et al. (2017)) as a function of earthquake magnitude, and (b) postseismic processes (the sum of interseismic relaxation and flexural-isostatic compensation). For (a), we set  $\theta = 45^\circ$ ,  $1/\beta = 1$ ,  $S_{mod} = 30^\circ$ ,  $\delta_{SN} = 1$ , and assume that landslides are mainly triggered by 1-Hz (period = 1 s) seismic waves.  $R_0$  is assumed to be equivalent to the fault depth (fault width  $\times \sin\theta$ ) for simplicity (Marc, Hovius, Meunier, Gorum, et al., 2016). Fault width is calculated using the scaling relations in Leonard (2010). For (b), we test earthquake magnitudes from 5 to 9 and the trends maintain similar, with varying  $T_e$  and other parameters same as in (a).

encompassing faults and earthquakes of varying sizes, the fault-produced topography should be composed of a series of topographic features with varying wavelength that is linked to fault characteristics. Aging, mature faults that are capable of generating fewer, higher magnitude, and deeper earthquakes are expected to produce longer-wavelength, smoothed topography, whereas younger, less mature faults (e.g., Wesnousky, 1994; Ben-Zion, 2008) are inclined to produce shorter wavelength, higher-relief, steeper topography at a faster pace.

## 7. Aseismic Processes and the Influence on the Volume Balance Over Earthquake Cycles

Equation (13) and the deformation partitioning coefficient  $f$  help us to evaluate the role of aseismic uplift in the volume balance over earthquake cycles. Based on equation (13), we calculate  $\Omega^*/\Omega$  as a function of  $f$  for varying isostatic compensation ( $\lambda$ ) and seismic volume balance ratio ( $\Omega$ ). As shown in Figure 12,  $\Omega^*/\Omega$  (volume balance ratio accounting for both seismic and aseismic uplift:seismic volume balance ratio) generally increases as  $f$  increases. As  $f$  approaches 1,  $\Omega^*/\Omega$  becomes less sensitive to change in  $f$ . For a given  $f$ ,  $\Omega^*/\Omega$  gets further away from 1 both as  $\lambda$  and  $\Omega$  decreases (Figures 12a and 12b), suggesting that aseismic slip can affect the overall volume balance significantly in cases when isostatic compensation is weak (low  $\lambda$ ) and/or landslide erosion counteracts little uplift (low  $\Omega$ ). Alternatively, for a given long-term tectonic uplift rate over earthquake cycles, higher  $f$  indicates more contribution to topography from seismic processes that trigger landslides, thus meaning relatively more landslide erosion as compared to low  $f$  scenarios.

Although there is no direct measurement of  $f$  in real geological settings, we use seismic coupling coefficient,  $\chi$ , defined as the ratio of seismic slip versus long-term slip, as a first-order approximation of  $f$ . Previous studies have compiled seismic coupling coefficients in typical tectonic settings and in major convergent plate boundary systems (e.g., Ader et al., 2012; Bird & Kagan, 2004; Li, West, et al., 2018; Scholz & Campos, 2012; Stevens & Avouac, 2015; Stirling et al., 2012; Theunissen et al., 2010; Wang et al., 2010), and we report those values in Figures 12c and 12d. In regions of high interseismic coupling (e.g., the Himalayas and the eastern Tibetan Mountains), for example, where we assert that  $f$  is close to 1, the corresponding  $\Omega^*/\Omega$  is predicted to be close to 1 as well (Figures 12a and 12b), meaning limited influence from aseismic slip on the total volume balance over earthquake cycles. If interseismic coupling is low and aseismic uplift is significant, the seismic volume balance ratio  $\Omega$  can be corrected to  $\Omega^*$  using equation (13) with the related parameters constrained. We also note that in typical continental convergent boundaries where mountainous topography is pronounced (e.g., the Himalayas),  $\chi$  and  $f$  are in general higher and closer to 1 than in other settings

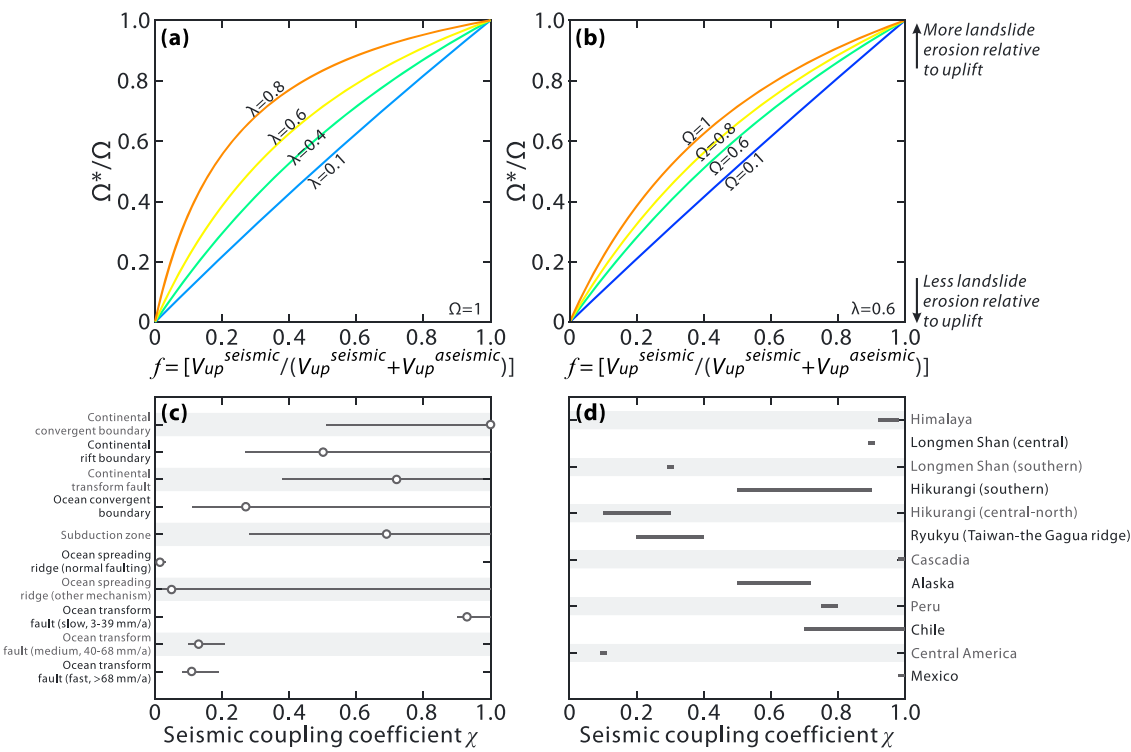


**Figure 12.**  $\Omega^*/\Omega$  (volume balance ratio accounting for both seismic and aseismic uplift:seismic volume balance ratio) as a function of  $f$ , the proportion of seismically induced uplift relative to the total uplift caused by seismic and aseismic deformations over one seismic cycle, under changing (a) isostatic response coefficient  $\lambda$  and (b) seismic volume balance ratio  $\Omega$ . Although there are no direct measurements of  $f$ , we use the seismic coupling coefficient  $\chi$ , the proportion of seismic slip over long-term slip, as a first-order approximation of  $f$ . (c) The  $\chi$  values in typical tectonic settings as compiled by Bird and Kagan (2004), with error bars indicating 95% confidence intervals. (d) The  $\chi$  values in major tectonically compressional regions and convergent plate boundary systems with error bars indicating uncertainties from spatial variations and/or calculation method: the Himalayas (Ader et al., 2012); the Longmen Shan mountain range at the eastern margin of the Tibetan Plateau (Li, West, et al., 2018); the Hikurangi subduction system (Stirling et al., 2012); the Ryukyu subduction system (Taiwan-Gagua ridge; Theunissen et al., 2010); Cascadia, Alaska, Chile, and Mexico (Scholz & Campos, 2012); and the Central America as an example of low  $\chi$  region (Scholz & Campos, 2012).

(Figures 12c and 12d), pointing to a major role of earthquakes in building topography in these environments. Yet we also recognize, as noted above, that many of these settings may be characterized by interseismic deformation associated with tectonic loading, which our model does not consider. Overall, although our analysis focuses on the volume budget and balance caused by seismic processes,  $f$  and  $\chi$  allow us to also account for aseismic uplift and thus provide a more comprehensive picture of deformation across earthquake cycles in diverse settings.

## 8. Topographic Effects of Earthquake Cycles at the Eastern Margin of the Tibetan Plateau

We apply our model to the central Longmen Shan Mountains where the 2008  $M_w 7.9$  Wenchuan earthquake occurred, to evaluate how earthquakes drive topographic evolution at the eastern margin of the Tibetan Plateau. We neglect aseismic processes in this analysis, because the seismogenic fault is thought to have been fully locked before the Wenchuan earthquake (Wang et al., 2010), and we consider this to be a region where the assumption of minimal effects from interseismic tectonic loading may be justified (see above). We first delineate the deformation field associated with the Wenchuan event, combining observational data of coseismic deformation and landslide erosion, along with modeling of interseismic deformation. For seismic deformation, we focus on the vertical displacement caused by the thrust component and neglect the strike-slip component which causes little vertical changes, although the Wenchuan earthquake contained both components (Hubbard, & Shaw, 2009; Liu-Zeng et al., 2009; Xu et al., 2009).

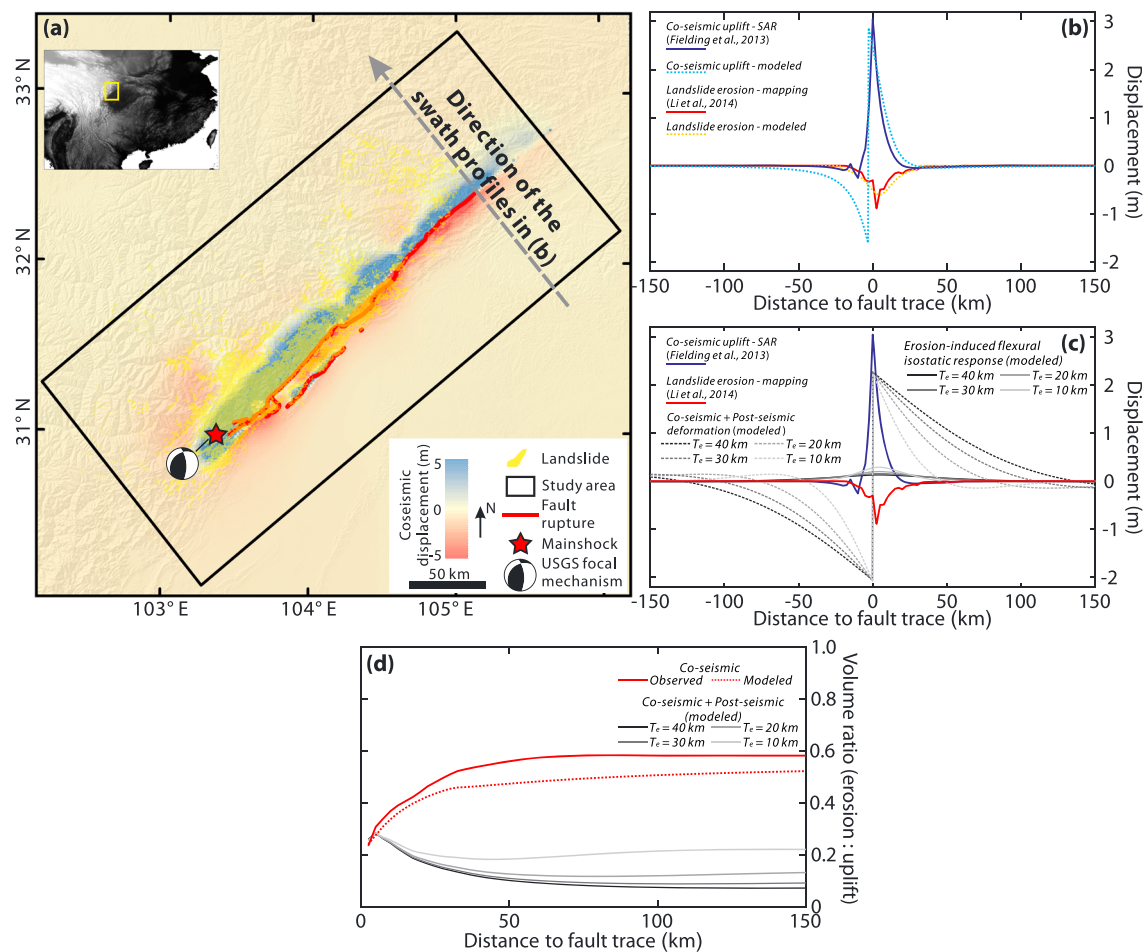


**Figure 13.** Spatial variations of seismically induced deformations for the 2008  $M_w7.9$  Wenchuan case. (a) Map view of the epicentral region of the Wenchuan earthquake, with coseismic displacement and ke-triggered landslides. (b) Vertical displacement caused by coseismic deformation and landslide erosion derived from observations and modeling. Model parameters are determined from the Wenchuan field data, with  $\theta = 65^\circ$ ,  $1/\beta = 0.68$ ,  $S_{mod} = 31^\circ$ ,  $\delta_{sn} = 5$ ,  $R_0 = 9.5$  km, assuming 1-Hz seismic waves are the main seismological factor responsible for triggering landsliding (Li et al., 2017; Li, West, et al., 2018; Liu-Zeng et al., 2009; Marc, Hovius, Meunier, Gorum, et al., 2016; Xu et al., 2009). (c) Displacement of seismically induced deformations (coseismic deformation, landslide erosion, combined coseismic and postseismic deformation, flexural isostatic response to landslide erosion) projected along the direction perpendicular to the fault trace, that is, the gray arrow in (a). (d) Volume ratio between landslide erosion and seismically induced uplift on the hanging wall for the observed and modeled coseismic case (solid and dashed red curves, respectively) and over the full earthquake cycle (gray curves) versus the distance to fault trace, with  $T_e$  of 10, 20, 30, and 40 km.

The observations from the Wenchuan earthquake illustrate well the distinct spatial patterns of seismically induced deformations (Figure 13), as predicted by our model: landslide erosion and coseismic deformation (both from empirical observations for this event) focus in a narrow corridor ( $<50$  km) above the fault plane and decay quickly away from the fault trace. Specifically comparing the empirical and model results, the magnitude and pattern of observed earthquake-triggered landslides match well with the results predicted from our model (Figure 13b). For coseismic deformation, our model reproduces the structure on the hanging wall, but lacks accuracy on the footwall (Figure 13b). Whereas geodetic observations show limited subsidence in this case (de Michele et al., 2010; Fielding et al., 2013), our adopted coseismic deformation model (Cohen, 1996) and other similar models based on uniform viscoelastic half space (King et al., 1988; Marc, Hovius, & Meunier, 2016; Okada, 1992; Thatcher & Rundle, 1984) predict major subsidence in the near field of the footwall. The discrepancy compared to observations is likely caused by the fact that in the case of the Wenchuan earthquake there is a strong contrast in lithospheric rheology between the hanging wall block (the Tibetan Plateau) and the footwall block (the Sichuan Basin, an ancient, intact carton whose viscosity is over 2 orders of magnitudes higher than the adjacent Tibetan block; Huang et al., 2014, and references

therein), which contradicts the assumption of homogeneous visco-elastic half space of the model. Moreover, numerical studies suggest that simple flexural-based models are not sufficient to explain footwall foreland basin subsidence, since more complex fault slip-basin margin interaction processes play an important role (e.g., Simpson, 2014). Such effects are also not considered in our model. However, our model reproduces well the features on the hanging wall, where landslide erosion and topographic uplift are mainly located, and we focus on these wall results in the following discussion.

We lack empirical data to compare to the modeled postseismic deformation and isostatic response, but the calculated values suggest that these distribute over much broader areas with much slower spatial decaying trends than the coseismic uplift or landslide erosion (Figure 13c).

To illustrate how the resulting Wenchuan earthquake volume balance varies spatially, we plot the volume balance ratio as a function of area in which the budget is calculated, which we define based on the distance to the fault trace (Figure 13d). We consider only the hanging wall results as discussed above (Figure 13d). Notably, the modeled coseismic volume ratio curve shows a similar trend as that derived from empirical observations, with around 10% difference in magnitude (Figure 13d). The coseismic volume ratio curve quickly saturates within a narrow zone near fault (<30 km) and changes little beyond this zone, as suggested by Marc, Hovius, and Meunier (2016). The postseismic curves decay continuously, extending to the far field (Figure 13d). Overall, the significant variation of the earthquake volume balance ratio over different integration boundaries demonstrates the importance of considering both far-field and near-field windows when interpreting the model results over earthquake cycles, whereas a near-field window is likely sufficient for capturing coseismic deformation alone. The Wenchuan example shows that considering postseismic in addition to coseismic processes can considerably change the inferred volume balance, with a greater difference in the far field and relatively smaller difference in the near field—emphasizing the role of postseismic processes in affecting the spatial distribution of deformation.

We next consider the topographic effects of multiple earthquake cycles in the eastern Tibetan Mountains. Whereas the field observations from the Wenchuan event help determine the parameters describing landscape susceptibility to landsliding and fault geometry (Li et al., 2017; Li, Zhang, et al., 2018; Liu-Zeng et al., 2009; Marc, Hovius, Meunier, Gorum, et al., 2016; Xu et al., 2009), major uncertainties exist in the effective elastic thickness ( $T_e$  ~7–40 km; Densmore et al., 2012; Fielding & McKenzie, 2012; Huang et al., 2014; Jordan & Watts, 2005) and earthquake depth ( $R_0$ , typically within 20-km depth in this region; Xu et al., 2009). To account for these uncertainties, in our modeling, we conduct Monte Carlo random sampling of  $T_e$  and  $R_0$  for each earthquake magnitude bin ( $M_w$ ~5–8 and  $\Delta M_w = 0.1$ ) and report the medians and the 16th and 84th percentiles of  $\Omega$  over earthquake magnitude for 1,000 simulations (Figure 14a). Here we only consider the near-field scenario to account for the mountainous region on the hanging wall. To integrate the effects over multiple earthquake cycles, we generate earthquake sequences using the earthquake frequency-magnitude relation established from the regional seismic catalog and paleoseismic studies (Li et al., 2017, and references therein). Note that the earthquake frequency-magnitude relation varies as a function of the different estimates of the recurrence time ( $T$ ) of Wenchuan-like events. We then calculate an average near-field volume balance ratio  $\Omega$  for all earthquake events of varying magnitudes, weighted by the total seismic uplift volume of each magnitude bin, that is, the product of earthquake occurrence time and the corresponding seismic uplift volume for a single event of the specified  $M_w$ .

As shown in Figure 14b, the uplift volume-weighted distribution of  $\Omega$  varies slightly across different estimated recurrence interval of the Wenchuan-like events ( $T$ ). Across the range of reported  $T$  values (500–4,000 years), we find that the net topographic effect of earthquake cycles tends to be constructive, with >95% probability for  $\Omega < 1$  and <5% probability for  $\Omega > 1$ . Using a similar approach, we also calculated the volume balance for coseismic scenarios (Figures 14c and 14d;  $\Omega_{\text{coseismic}} = V_{ls}/V_{up}^{\text{coseismic}}$ ). Compared to the volume balance over full earthquake cycles, we find that considering only the coseismic components, earthquakes tend to be more erosive (with 10–30% probability of being net destructive; Figure 14d), and this difference clearly demonstrates the buffering role of interseismic processes in regulating seismically produced topography. Overall, at the eastern margin of the Tibetan Plateau, our analysis suggests that earthquakes work mainly as topographic constructors over multiple seismic cycles, even though the Wenchuan earthquake stimulated interest in this problem due to its highly erosive characteristics (Figure 14b).

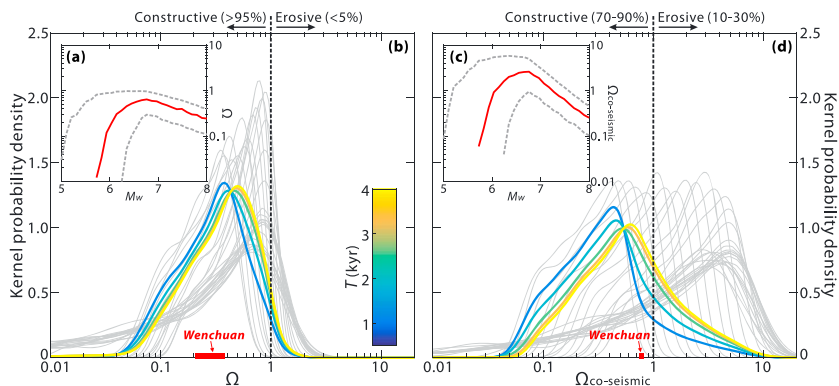


**Figure 14.** Volume balance and the overall topographic effects of earthquake cycles at the eastern margin of the Tibetan Plateau modeled via Monte Carlo random sampling of  $T_e$  (7–40 km) and  $R_0$  (1–20 km) for earthquake events with  $M_w \sim 5$ –8. Other model parameters are determined from the Wenchuan field data, considering hanging wall, near-field scenarios. (a) Seismic volume balance ratio ( $\Omega$ , landslide erosion: uplift) versus  $M_w$ : 1,000 times' Monte Carlo simulations are run for each earthquake magnitude bin ( $\Delta M_w = 0.1$ ) to account for variations of  $T_e$  and  $R_0$ ; the results are reported as the medians (red solid curve) and an envelope bounded by the 16th–84th percentiles (gray dashed curves) of the modeled  $\Omega$  population. (b) Kernel probability density of  $\Omega$  for each earthquake magnitude bin (gray curves, with each curve representing the probability density for the 1,000  $\Omega$  values from the Monte Carlo simulations for a specified  $M_w$  bin) and for the average of  $\Omega$  weighted by seismic uplift and occurrence frequency of each  $M_w$  bin (colored curves) considering different estimates of the recurrence time of Wenchuan-like events,  $T$ , as indicated by the colored curves and the color bar. Our results suggest the overall topographic effect of earthquake cycles tends to be constructive (with >90% probability for  $\Omega < 1$ ) rather than erosive (with <10% probability for  $\Omega > 1$ ). The red bar indicates the Wenchuan event. (c and d) Co-seismic scenarios ( $\Omega_{\text{coseismic}} = V_{ls}/V_{up}^{\text{coseismic}}$ ), with the red square on (d) representing the Wenchuan case.

## 9. Conclusions, Limitations, and Implications

Taking a modeling approach, we have evaluated the volume balance between tectonic uplift and landslide erosion over earthquake cycles, considering varying magnitudes and different seismotectonic and topographic conditions and extensively exploring the relevant parameter space. Several findings contribute to better understanding of the seismic role in mountain building:

1. The extent to which earthquakes build or destroy mountains depends on earthquake magnitudes, topographic and seismotectonic conditions, and assumptions about the seismological triggering of landslides. At the eastern margin of the Tibetan Plateau where the 2008 Wenchuan earthquake occurred, across the currently known ranges of the related parameters and the possible mechanisms triggering landslides, we conclude that the long-term effect of earthquakes tends to be topographic construction, and that destructive events are rare (e.g., Figure 14b). Nonetheless, although most are likely not to be net destructive, the erosive power of earthquakes may play a significant role in topographic evolution, particularly by affecting the location and spatial distribution of deformation.
2. Different processes operating over one full earthquake cycle produce topographic forms of distinct spatial patterns. Landslide erosion and coseismic deformation are focused on a narrow window near the fault trace, but postseismic relaxation and erosion-induced isostatic uplift distribute deformation over broader areas. Thus, understanding of the earthquake volume balance depends on defining a spatial window, and one-dimensional calculations may overlook the fact that spatially nonuniform deformation can shape the resulting topographic features. Aseismic slip can also contribute to long-term uplift, and can be accounted for in the overall volume balance using a deformation partitioning coefficient, although the influence of aseismic deformation is expected to be limited in regions with high interseismic coupling, such as the Himalayas and the eastern margin of the Tibetan Plateau.
3. We confirm previous findings (Li et al., 2014; Marc, Hovius, & Meunier, 2016) that earthquake magnitude exerts a primary control on the volume of earthquake-triggered landslides and seismically uplifted topography, and thus on the related volume balance ratio. Seismotectonic and topographic conditions modulate volumes of seismically induced deformations but have a secondary influence on the overall budget, except in cases where landscapes have very limited susceptibility of landsliding (e.g., low steepness). Larger landslide volumes and more erosive earthquake events tend to occur in seismic zones

characterized by shallower rupture depths and thinner effective elastic thickness, and in steeper and more landslide-prone landscapes.

4. Assumptions about the seismological factor that is most relevant to landslide triggering lead to large uncertainties in modeled landslide volume and volume ratio, highlighting the importance of better understanding of landsliding-triggering mechanisms. The assumed landsliding-triggering factor also dictates the patterns of  $V_{ls}$ - $M_w$  and  $\Omega$ - $M_w$  relations. As  $M_w$  increases,  $\Omega$  either peaks around the hinge magnitude beyond which ground motion saturates, or increases monotonically with  $M_w$ , depending on the assumed landslide-triggering factor.
5. Seismically uplifted or eroded topography represents the geomorphic work done by earthquakes using the released seismic moment. At higher earthquake magnitudes, earthquakes erode and uplift less volume per unit seismic moment, meaning they are less efficient in driving topographic change. This relationship is caused by the saturation of ground motion approaching higher magnitude and the lower dependence on fault width that determines the horizontal wavelength of the seismically uplifted topography. However, when considering the relative contributions to the total volume budget, we find that higher-magnitude earthquakes contribute more to total seismic uplift, whereas medium-to-high-magnitude earthquakes contribute most to landslide erosion.
6. Over full earthquake cycles, the wavelength of seismically created topography to first-order scales with  $T_e$ , earthquake magnitude, and fault dimensions. These findings provide a mechanistic link between fault characteristics, seismicity, and topography. We hypothesize that aging, mature fault systems that can generate higher-magnitude earthquakes are capable of producing longer wavelength, smoothed topography, whereas less mature faults tend to create shorter-wavelength, higher-relief, steeper topography.

Despite these new understanding gained from our modeling effort, several limitations exist in this work, and these limitations point to key directions of further research.

1. As we neglect interseismic loading, our model does not fully represent the processes active in regions where interseismic processes contribute significantly to surface deformation (e.g., the Himalayas and Taiwan), although our model does capture the coseismic and postseismic components and is expected to apply to settings where interseismic loading is applied at regional scales (e.g., eastern Tibet). As we focus on seismic processes, we simplify aseismic processes using a deformation partitioning coefficient. Since aseismic processes can also play an important role in long-term uplift in some settings (Simpson, 2015; Marc, Hovius, & Meunier, 2016), more detailed modeling of aseismic processes considering different modes of creeping and loading (e.g., regional versus localized; Johnson et al., 2005; Simpson, 2015) could add further insight, as could modeling of tectonic leading coupled to episodic seismically triggered erosion.
2. With the shortcomings of our 2-D approach, our model captures single seismic cycles only for high-magnitude earthquakes with long rupture length ( $L/T_e > \sim 10$ ) and long recurrence time (e.g.,  $> 10$  times of Maxwell relaxation time  $\tau$ ), or multiple earthquake cycles when the tectonic setting satisfies the above rules. Applying the model to single smaller-magnitude events with lower fault length-to- $T_e$  ratios could be problematic. The 2-D approach also limits our understanding of the 3-D structures of seismically induced deformation and how along-strike variations influence on the seismic volume budget. 3-D models in future studies could address these issues (e.g., Ren et al., 2018; Sun et al., 2014).
3. Our model is based on homogeneous viscoelastic half space, so will not completely represent regions with heterogeneous rheology such as the eastern Tibetan margin, where our results perform poorly in replicating the observed footwall deformation associated with the Wenchuan earthquake. Moreover, we have not considered the role of sedimentation and fault slip in range-bounding basins (e.g., Densmore et al., 2012; King et al., 1988; Simpson, 2014), which should have major influence in range-basin settings. In the context of our modeling framework, adding a sedimentation component in the footwall basins would both reduce footwall subsidence (because of sediment infill) and the adjacent hanging wall uplift due to flexural isostatic response to loading, but the net effect remains unconstrained. To better constrain the role of basin sedimentation in earthquake volume balance, future studies are needed to better describe how sediments are distributed in range-front basins, which likely vary as functions of fluvial sediment transport and the basin properties (e.g., geometry, structure, and rheology) (Huang et al., 2014, and references therein). Recent studies also highlight the importance of the kinematics of basin margins related to fault slip and lithospheric deformation in basin subsidence

(Simpson, 2014), which should be considered as well. However, we do not expect that including the sedimentation component would affect our major interpretations that earthquake sequences tend to be topographically constructive in settings like the eastern Tibetan Mountains, and that landslide erosion can affect topographic wavelength.

4. We do not consider the evolution of relief with time, as in a landscape evolution model, or the effect of geomorphic transport processes driven by climatic variations (Perron, 2017; Whipple, 2009). Neither do we account for the transient changes of landslide propensity in response to climatic triggers during postearthquake time periods (e.g., Marc et al., 2015; Parker et al., 2015), which are also important in determining of how earthquakes work to influence landscape erosion. Thus, we cannot simulate how fault systems, earthquake cycles, and mountainous landscapes coevolve over time.

Overall, although our model has these many shortcomings and simplifications, our results have meaningful implications. One the one hand, we find that, especially when considering the modulating effect of postseismic processes, the vast majority of large earthquakes in a setting such as the eastern margin of the Tibetan Plateau are likely constructive—dispelling any apparent paradox in which large earthquake might be thought of as “net erosive.” At the same time, our results suggest that the erosive component of earthquakes can be important in shaping first-order features of large-scale topography, especially considering the evolving characteristics of fault systems and how these characteristics may affect patterns of erosion versus uplift. Thus episodic, seismically induced landslides erosion should be considered in more complete models of landscape evolution and crustal deformation over earthquake cycles, particularly considering the cumulative effect of multiple faults of varying maturity.

## Symbol Notations

$A$	Fault rupture area, $\text{km}^2$
$a$	Local peak ground seismic acceleration, gravitational acceleration $g$
$a_c$	Threshold acceleration to landsliding, gravitational acceleration $g$
$A_{topo}$	Fraction of topography available for landsliding, dimensionless
$b$	Inferred acceleration at 1 km from seismic energy source for a given landslide-triggering mechanism, gravitational acceleration $g$
$b_{sat}$	Saturated acceleration of $b$ , gravitational acceleration $g$
$d$	Distance to seismic energy source, km
$D$	Fault displacement, km
$E$	Young's modulus, Pa
$f$	Partitioning coefficient of deformation over earthquake cycles, dimensionless
$e_5, e_6, e_7$	Empirical scaling parameters for ground motion, dimensionless
$I_{asp}$	Seismic energy spot length scale, km
$L$	Fault rupture length, km
$L_{sf}$	Fault surface rupture length, km
$M_o$	Seismic moment, $\text{N} \cdot \text{m}$
$M_w$	Moment magnitude, dimensionless
$P_0$	Scaling parameter for predicting landslide pattern, $\text{m}^3/\text{km}^2$
$P_{Vls}$	Landslide volumetric density, $\text{m}^3/\text{km}^2$
$R_o$	Mean asperity depth, km
$R_{ref}$	Reference distance, km
$S$	Site effect on amplification of ground motion, dimensionless
$\bar{S}$	Average site effect on amplification of ground motion, dimensionless
$S_{mod}$	Landscape modal slope, deg
$\tau$	Maxwell relaxation time, year
$T$	Recurrence time of Wenchuan-like events, year
$T_e$	Lithospheric effective elastic thickness, km
$T_{sv}$	Empirical steepness normalization constant, deg
$V_{ls}$	Landslide volume, $\text{km}^3$

$V_{\text{up}}$	Total uplift volume, km <sup>3</sup>
$V_{\text{up}}^{\text{aseismic}}$	Aseismically uplifted volume, km <sup>3</sup>
$V_{\text{up}}^{\text{isostasy}}$	Isostatically uplifted volume induced by landslide erosion, km <sup>3</sup>
$V_{\text{up}}^{\text{seismic}}$	Seismically uplifted volume, km <sup>3</sup>
$W$	Fault width, km
$W_f$	Width of far-field window, km
$W_n$	Width of near-field window, km
$\beta$	Landslide spatial pattern factor, dimensionless
$\delta_{sn}$	Normalized landscape failure susceptibility, dimensionless
$\delta_V$	Landscape failure susceptibility, m <sup>3</sup> /km <sup>2</sup>
$\bar{\delta}v$	Global-averaged landscape failure susceptibility, m <sup>3</sup> /km <sup>2</sup>
$\theta$	Fault dip, deg
$\lambda$	Ratio between $V_{\text{up}}^{\text{isostasy}}$ and $V_{ls}$ , dimensionless
$\mu$	Shear modulus, Pa
$\nu$	Poisson ratio, dimensionless
$\rho_A$	Density of asthenosphere, kg/m <sup>3</sup>
$\rho_L$	Density of lithosphere, kg/m <sup>3</sup>
$\Omega$	Seismic volume balance ratio, dimensionless
$\Omega^*$	Volume balance ratio over full earthquake cycles accounting for uplift driven by both seismic and aseismic processes, dimensionless
$\Omega_{\text{coseismic}}$	Coseismic volume balance ratio (landslide erosion:coseismic uplift), dimensionless
$\bar{\Omega}$	Average volume balance ratio over the sampling parameter space

## Appendix A

In Appendix A, we present the contour plots of the relative earthquake volume balance ratio (defined as the difference between the earthquake volume balance ratio and the average volume balance ratio) over the parameter space for various earthquake magnitudes and a more complete set of landslide-triggering factors (Figures A1, A2, A3, and A4).

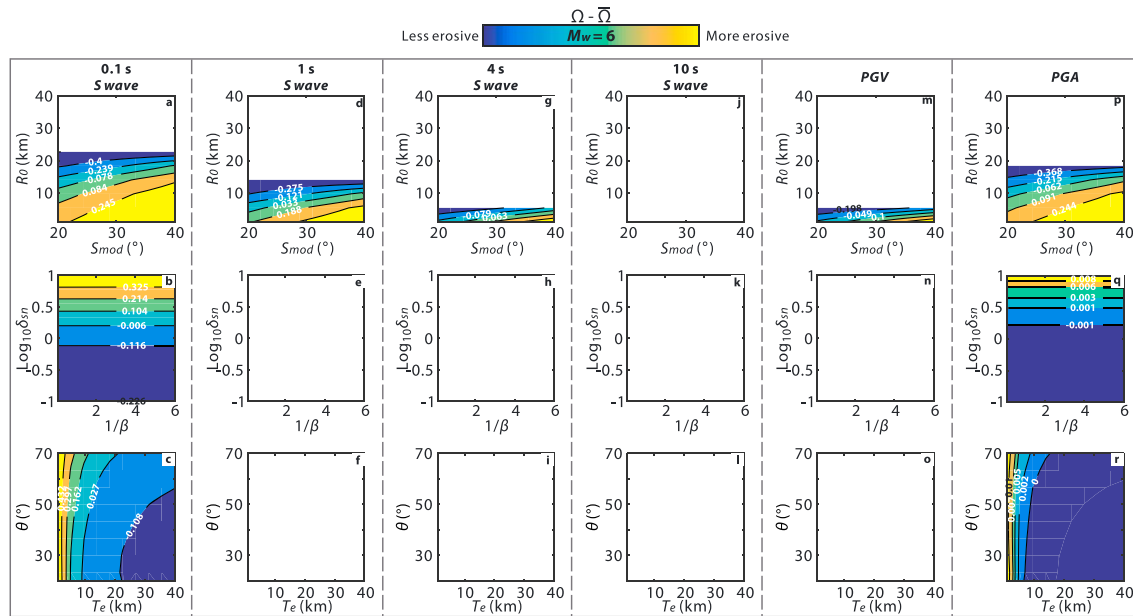


**Figure A1.** Contour plots of the relative earthquake volume balance ratio, defined as the difference between the earthquake volume balance ratio  $\Omega$  and the average volume balance ratio  $\bar{\Omega}$  over the sampling space. We consider  $M_w = 6$  here and a range of seismological factors (S waves of different periods, PGV and PGA) responsible for triggering landslides in a far-field scenario. Blank areas represent no landslides being triggered for the given conditions.

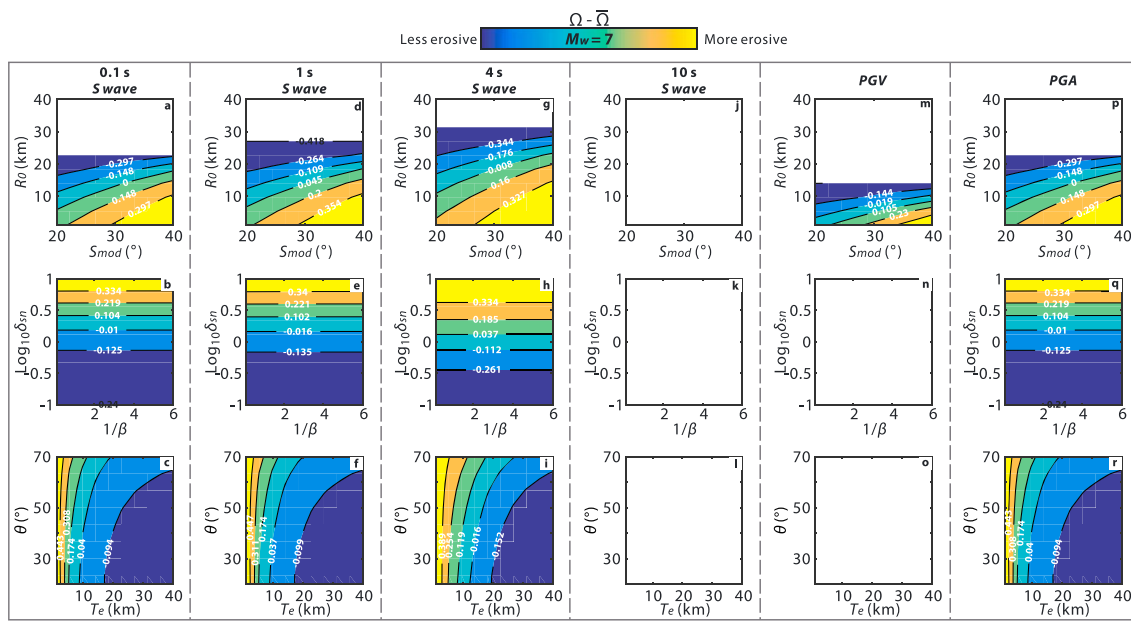


**Figure A2.** Contour plots of the relative earthquake volume balance ratio, defined as the difference between the earthquake volume balance ratio  $\Omega$  and the average volume balance ratio  $\bar{\Omega}$  over the sampling space. We consider  $M_w = 7$  here and a range of seismological factors ( $S$  waves of different periods, PGV and PGA) responsible for triggering landslides in a far-field scenario. Blank areas represent no landslides being triggered for the given conditions.

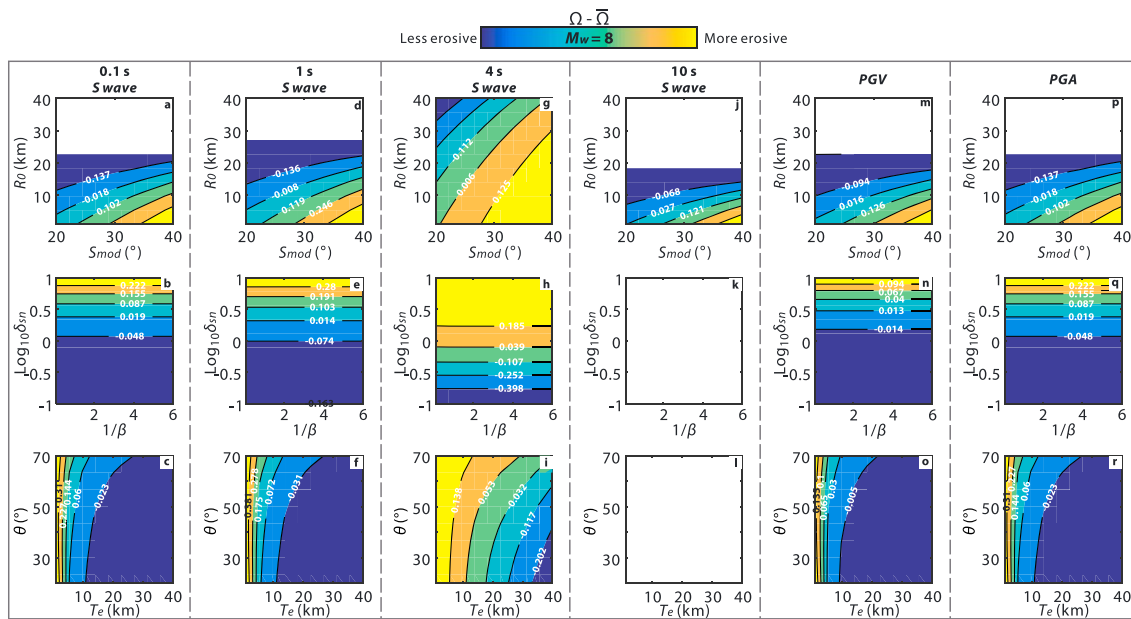


**Figure A3.** Contour plots of the relative earthquake volume balance ratio, defined as the difference between the earthquake volume balance ratio  $\Omega$  and the average volume balance ratio  $\bar{\Omega}$  over the sampling space. We consider  $M_w = 8$  here and a range of seismological factors ( $S$  waves of different periods, PGV and PGA) responsible for triggering landslides in a far-field scenario. Blank areas represent no landslides being triggered for the given conditions.

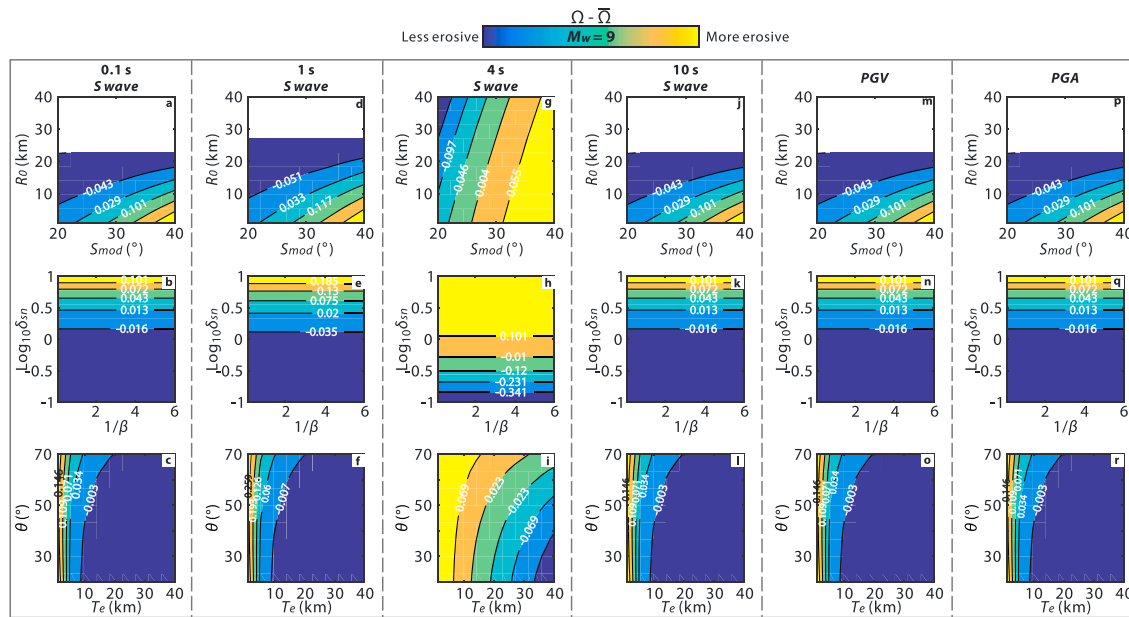


**Figure A4.** Contour plots of the relative earthquake volume balance ratio, defined as the difference between the earthquake volume balance ratio  $\Omega$  and the average volume balance ratio  $\bar{\Omega}$  over the sampling space. We consider  $M_w = 9$  here and a range of seismological factors ( $S$  waves of different periods, PGV and PGA responsible for triggering landslides in a far-field scenario. Blank areas represent no landslides being triggered for the given conditions.

## Acknowledgments

This work was funded by the U.S. National Science Foundation (NSF-EAR/GLD grants 1053504 and 1640894 to A.J.W.). G.L. was supported by a USC Dornsife college graduate merit fellowship. We thank Jean-Philippe Avouac, Sylvain Barbot, Alexander Densmore, Josh Roering, Niels Hovius, Odin Marc, Patrick Meunier, Yehuda Ben-Zion, James Dolan, Luca Dal Zilio, Lei Qin, Haoran Meng, Chris Milliner, Zhigang Peng, Mong-Han Huang, Lingsen Meng, and Joel Scheingross for their helpful discussions. G.L. thanks Wanbin Chen for the discussions about several mathematical problems involved in this work. We thank three reviewers and the Editor for their insightful and constructive comments that helped to improve an earlier version of the manuscript, and we appreciate the editorial handling. This paper is mainly built on the results from a numerical model, and the adopted Wenchuan seismic deformation and landslide data are contained in multiple published sources cited in references.

## References

- Ader, T., Avouac, J.-P., Liu-Zeng, J., Lyon-Caen, H., Bollinger, L., Galetzka, J., et al. (2012). Convergence rate across the Nepal Himalaya and interseismic coupling on the Main Himalayan Thrust: Implications for seismic hazard. *Journal of Geophysical Research*, 117, B04403. <https://doi.org/10.1029/2011JB009071>
- Athanasiopoulos-Zekkos, A., Pence, H., & Lobbestael, A. (2016). Ground Motion Selection for Seismic Slope Displacement Evaluation Analysis of Earthen Levees. *Earthquake Spectra*, 32(1), 217–237.
- Avouac, J. P. (2007). 6.09—Dynamic Processes in Extensional and Compressional Settings—Mountain Building: From Earthquakes to Geological Deformation. In S. Gerald (Ed.), *Treatise on Geophysics* (pp. 377–439). Amsterdam: Elsevier.
- Barlow, J., Barisin, I., Rosser, N., Petley, D., Densmore, A., & Wright, T. (2015). Seismically-induced mass movements and volumetric fluxes resulting from the 2010  $M_w 7.2$  earthquake in the Sierra Cucapah, Mexico. *Geomorphology*, 230(0), 138–145.
- Ben-Zion, Y. (2008). Collective behavior of earthquakes and faults: Continuum-discrete transitions, progressive evolutionary changes, and different dynamic regimes. *Reviews of Geophysics*, 46, RG4006. <https://doi.org/10.1029/2008RG000260>
- Bird, P., & Kagan, Y. Y. (2004). Plate-Tectonic Analysis of Shallow Seismicity: Apparent Boundary Width, Beta, Corner Magnitude, Coupled Lithosphere Thickness, and Coupling in Seven Tectonic Settings. *Bulletin of the Seismological Society of America*, 94(6), 2,380–2,399.
- Bollinger, L., Sapkota, S. N., Tapponnier, P., Klinger, Y., Rizza, M., Van der Woerd, J., et al. (2014). Estimating the return times of great Himalayan earthquakes in eastern Nepal: Evidence from the Patu and Bardibas strands of the Main Frontal Thrust. *Journal of Geophysical Research: Solid Earth*, 119, 7123–7163. <https://doi.org/10.1002/2014JB010970>
- Boore, D. M., & Atkinson, G. M. (2008). Ground-Motion Prediction Equations for the Average Horizontal Component of PGA, PGV, and 5%-Damped PSA at Spectral Periods Between 0.01 s and 10.0 s. *Earthquake Spectra*, 24(1), 99–138.
- Boos, W. R., & Kuang, Z. (2010). Dominant control of the South Asian monsoon by orographic insulation versus plateau heating. *Nature*, 463(7278), 218–222.
- Brenguier, F., Campillo, M., Hadzioannou, C., Shapiro, N. M., Nadeau, R. M., & Larose, E. (2008). Postseismic Relaxation Along the San Andreas Fault at Parkfield From Continuous Seismological Observations. *Science*, 321(5895), 1,478–1,481.
- Burchfiel, B. C., Royden, L. H., van der Hilst, R. D., Hager, B. H., Chen, Z., King, R. W., et al. (2008). A geological and geophysical context for the Wenchuan earthquake of 12 May 2008, Sichuan, People's Republic of China. *GSA Today*, 18(7), 5.
- Burov, E. B., & Diament, M. (1995). The effective elastic thickness ( $T_e$ ) of continental lithosphere: What does it really mean? *Journal of Geophysical Research*, 100(B3), 3905–3927.
- Cattin, R., & Avouac, J. P. (2000). Modeling mountain building and the seismic cycle in the Himalaya of Nepal. *Journal of Geophysical Research*, 105(B6), 13,389–13,407.
- Clark, M. K., & Royden, L. H. (2000). Topographic ooze: Building the eastern margin of Tibet by lower crustal flow. *Geology*, 28(8), 703–706.
- Cohen, S. C. (1996). Convenient formulas for determining dip-slip fault parameters from geophysical observables. *Bulletin of the Seismological Society of America*, 86(5), 1,642–1,644.
- Croissant, T., Lague, D., Steer, P., & Davy, P. (2017). Rapid post-seismic landslide evacuation boosted by dynamic river width. *Nature Geoscience*, 10, 680.
- Dal Zilio, L., van Dinther, Y., Gerya, T., & Avouac, J.-P. (2019). Bimodal seismicity in the Himalaya controlled by fault friction and geometry. *Nature Communications*, 10(1), 48.

- de Michele, M., Raucoles, D., de Sigoyer, J., Pubellier, M., & Chamot-Rooke, N. (2010). Three-dimensional surface displacement of the 2008 May 12 Sichuan earthquake (China) derived from Synthetic Aperture Radar: evidence for rupture on a blind thrust. *Geophysical Journal International*, 183(3), 1097–1103.
- Densmore, A. L., Parker, R. N., Rosser, N. J., de Michele, M., Li, Y., Huang, R. Q., et al. (2012). Isostasy can't be ignored reply. *Nature Geoscience*, 5(2), 83–84.
- Dreyfus, D., Rathje, E. M., & Gibson, R. W. (2013). The influence of different simplified sliding-block models and input parameters on regional predictions of seismic landslides triggered by the Northridge earthquake. *Engineering Geology*, 163, 41–54.
- Elliott, J. R., Jolivet, R., González, P. J., Avouac, J. P., Hollingsworth, J., Searle, M. P., & Stevens, V. L. (2016). Himalayan megathrust geometry and relation to topography revealed by the Gorkha earthquake. *Nature Geoscience*, 9, 174.
- Fan, X., Domènec, G., Scaringi, G., Huang, R., Xu, Q., Hales, T. C., et al. (2018). Spatio-temporal evolution of mass wasting after the 2008  $M_w$  7.9 Wenchuan earthquake revealed by a detailed multi-temporal inventory. *Landslides*, 15(12), 2325–2341.
- Fielding, E. J., & McKenzie, D. (2012). Lithospheric flexure in the Sichuan Basin and Longmen Shan at the eastern edge of Tibet. *Geophysical Research Letters*, 39, L09311. <https://doi.org/10.1029/2012GL051680>
- Fielding, E. J., Sladen, A., Li, Z. H., Avouac, J. P., Burgmann, R., & Ryder, I. (2013). Kinematic fault slip evolution source models of the 2008  $M_w$  7.9 Wenchuan earthquake in China from SAR interferometry, GPS and teleshismic analysis and implications for Longmen Shan tectonics. *Geophysical Journal International*, 194(2), 1138–1166.
- Gallen, S. F., Clark, M. K., & Godt, J. W. (2015). Coseismic landslides reveal near-surface rock strength in a high-relief, tectonically active setting. *Geology*, 43(1), 11–14.
- Galy, V., France-Lanord, C., Beyssac, O., Faure, P., Kudrass, H., & Palhol, F. (2007). Efficient organic carbon burial in the Bengal fan sustained by the Himalayan erosional system. *Nature*, 450(7168), 407–U406.
- Gassenmeier, M., Sens-Schönfelder, C., Eulenfeld, T., Bartsch, M., Victor, P., Tilmann, F., & Korn, M. (2016). Field observations of seismic velocity changes caused by shaking-induced damage and healing due to mesoscopic nonlinearity. *Geophysical Journal International*, 204(3), 1,490–1,502.
- Godard, V., Cattin, R., & Lave, J. (2004). Numerical modeling of mountain building: Interplay between erosion law and crustal rheology. *Geophysical Research Letters*, 31, L23607. <https://doi.org/10.1029/2004GL021006>
- Godard, V., Cattin, R., & Lavé, J. (2009). Erosional control on the dynamics of low-convergence rate continental plateau margins. *Geophysical Journal International*, 179(2), 763–777.
- Gutenberg, B., & Richter, C. F. (1954). *Seismicity of the Earth and Associated Phenomenon* (2nd Ed.). Princeton, NJ: Princeton University Press.
- Hanks, T. C., & Kanamori, H. (1979). A moment magnitude scale. *Journal of Geophysical Research*, 84(B5), 2348–2350.
- Harp, E. L., & Gibson, R. W. (1996). Landslides triggered by the 1994 Northridge, California, earthquake. *Bulletin of the Seismological Society of America*, 86(1B), S319–S332.
- Hillers, G., Mai, P. M., Ben-Zion, Y., & Ampuero, J. P. (2007). Statistical properties of seismicity of fault zones at different evolutionary stages. *Geophysical Journal International*, 169(2), 515–533.
- Hovius, N. (1996). Regular spacing of drainage outlets from linear mountain belts. *Basin Research*, 8(1), 29–44.
- Hovius, N., Meunier, P., Ching-Weei, L., Hongey, C., Yue-Gau, C., Dadson, S., et al. (2011). Prolonged seismically induced erosion and the mass balance of a large earthquake. *Earth and Planetary Science Letters*, 304(3–4), 347–355.
- Hovius, N., Stark, C. P., & Allen, P. A. (1997). Sediment flux from a mountain belt derived by landslide mapping. *Geology*, 25(3), 231–234.
- Huang, M.-H., Bürgmann, R., & Freed, A. M. (2014). Probing the lithospheric rheology across the eastern margin of the Tibetan Plateau. *Earth and Planetary Science Letters*, 396, 88–96.
- Hubbard, J., & Shaw, J. H. (2009). Uplift of the Longmen Shan and Tibetan Plateau, and the 2008 Wenchuan ( $M = 7.9$ ) earthquake. *Nature*, 458(7235), 194–197.
- Jiang, J., & Lapusta, N. (2016). Deeper penetration of large earthquakes on seismically quiescent faults. *Science*, 352(6291), 1,293–1,297.
- Jibson, R. W., & Keefer, D. K. (1993). Analysis of the seismic origin of landslides: Examples from the New Madrid seismic zone. *Geological Society of America Bulletin*, 105(4), 521–536.
- Johnson, K. M., Segall, P., & Yu, S. B. (2005). A viscoelastic earthquake cycle model for Taiwan. *Journal of Geophysical Research*, 110, B10404. <https://doi.org/10.1029/2004JB003516>
- Jordan, T. A., & Watts, A. B. (2005). Gravity anomalies, flexure and the elastic thickness structure of the India–Eurasia collisional system. *Earth and Planetary Science Letters*, 236(3), 732–750.
- Keefer, D. K. (1994). The importance of earthquake-induced landslides to long-term slope erosion and slope-failure hazards in seismically active regions. *Geomorphology*, 10(1), 265–284.
- Kelsey, H. M. (1990). Late Quaternary deformation of marine terraces on the Cascadia Subduction Zone near Cape Blanco, Oregon. *Tectonics*, 9(5), 983–1,014.
- King, G. C. P., Stein, R. S., & Rundle, J. B. (1988). The Growth of Geological Structures by Repeated Earthquakes 1. Conceptual Framework. *Journal of Geophysical Research*, 93(B11), 13,307–13,318.
- Lee, W. H. K., Shin, T. C., Kuo, K. W., Chen, K. C., & Wu, C. F. (2001). CWB free-field strong-motion data from the 21 September Chi-Chi, Taiwan, earthquake. *Bulletin of the Seismological Society of America*, 91(5), 1,370–1,376.
- Leonard, M. (2010). Earthquake fault scaling: Self-consistent relating of rupture length, width, average displacement, and moment release. *Bulletin of the Seismological Society of America*, 100(5A), 1,971–1,988.
- Li, G., West, A. J., Densmore, A. L., Hammond, D. E., Jin, Z., Zhang, F., et al. (2016). Connectivity of earthquake-triggered landslides with the fluvial network: Implications for landslide sediment transport after the 2008 Wenchuan earthquake. *Journal of Geophysical Research: Earth Surface*, 121, 703–724. <https://doi.org/10.1002/2015JF003718>
- Li, G., West, A. J., Densmore, A. L., Jin, Z., Parker, R. N., & Hilton, R. G. (2014). Seismic mountain building: Landslides associated with the 2008 Wenchuan earthquake in the context of a generalized model for earthquake volume balance. *Geochemistry, Geophysics, Geosystems*, 15, 833–844. <https://doi.org/10.1002/2013GC005067>
- Li, G., West, A. J., Densmore, A. L., Jin, Z., Zhang, F., Wang, J., et al. (2017). Earthquakes drive focused denudation along a tectonically active mountain front. *Earth and Planetary Science Letters*, 472, 253–265.
- Li, G., West, A. J., Densmore, A. L., Jin, Z., Zhang, F., Wang, J., & Hilton, R. G. (2018). Distribution of earthquake-triggered landslides across landscapes: Towards understanding erosional agency and cascading hazards. In Y.-G. Li (Ed.), *Fault-Zone Guided Wave, Ground Motion, Landslide and 5180 Earthquake Forecast*, (pp. 160–190). Berlin, Boston: De Gruyter.
- Li, X., Zhou, Z., Yu, H., Wen, R., Lu, D., Huang, M., et al. (2008). Strong motion observations and recordings from the great Wenchuan earthquake. *Earthquake Engineering and Engineering Vibration*, 7(3), 235–246.

- Li, Y., Zhang, G., Shan, X., Liu, Y., Wu, Y., Liang, H., et al. (2018). GPS-Derived Fault Coupling of the Longmenshan Fault Associated with the 2008  $M_w$  Wenchuan 7.9 Earthquake and Its Tectonic Implications. *Remote Sensing*, 10(5), 753.
- Liu-Zeng, J., Zhang, Z., Wen, L., Tapponnier, P., Sun, J., Xing, X., et al. (2009). Co-seismic ruptures of the 12 May 2008,  $M_s$  8.0 Wenchuan earthquake, Sichuan: East-west crustal shortening on oblique, parallel thrusts along the eastern edge of Tibet. *Earth and Planetary Science Letters*, 286(3-4), 355–370. <https://doi.org/10.1016/j.epsl.2009.07.017>
- Maggi, A., Jackson, J. A., McKenzie, D., & Priestley, K. (2000). Earthquake focal depths, effective elastic thickness, and the strength of the continental lithosphere. *Geology*, 28(6), 495–498.
- Malamud, B. D., Turcotte, D. L., Guzzetti, F., & Reichenbach, P. (2004). Landslides, earthquakes, and erosion. *Earth and Planetary Science Letters*, 229(1–2), 45–59.
- Marc, O., Behling, R., Andermann, C., Turowski, J. M., Illien, L., Roessner, S., & Hovius, N. (2019). Long-term erosion of the Nepal Himalayas by bedrock landsliding: the role of monsoons, earthquakes and giant landslides. *Earth Surface Dynamics*, 7(1), 107–128.
- Marc, O., Hovius, N., & Meunier, P. (2016). The mass balance of earthquakes and earthquake sequences. *Geophysical Research Letters*, 43, 3708–3716. <https://doi.org/10.1002/2016GL068333>
- Marc, O., Hovius, N., Meunier, P., Gorum, T., & Uchida, T. (2016). A seismologically consistent expression for the total area and volume of earthquake-triggered landsliding. *Journal of Geophysical Research: Earth Surface*, 121, 640–663. <http://doi.org/10.1002/2015JF003732>
- Marc, O., Hovius, N., Meunier, P., Uchida, T., & Hayashi, S. (2015). Transient changes of landslide rates after earthquakes. *Geology*, 43(10), 883–886.
- Marc, O., Meunier, P., & Hovius, N. (2017). Prediction of the area affected by earthquake-induced landsliding based on seismological parameters. *Natural Hazards and Earth System Sciences*, 17(7), 1,159–1,175.
- Maufroy, E., Cotton, F., Cruz-Atienza, V. M., & Gaffet, S. (2014). Frequency-scaled curvature as a proxy for topographic site effect: amplification and ground motion variability. *Bulletin of the Seismological Society of America*, 105(1), 354–367.
- Meade, B. J. (2010). The signature of an unbalanced earthquake cycle in Himalayan topography? *Geology*, 38(11), 987–990.
- Meunier, P., Hovius, N., & Haines, A. J. (2007). Regional patterns of earthquake-triggered landslides and their relation to ground motion. *Geophysical Research Letters*, 34, L20408. <https://doi.org/10.1029/2007GL031337>
- Meunier, P., Hovius, N., & Haines, A. J. (2008). Topographic site effects and the location of earthquake induced landslides. *Earth and Planetary Science Letters*, 275(3–4), 221–232.
- Milliner, C. W. D., Sammis, C., Allam, A. A., Dolan, J. F., Hollingsworth, J., Leprince, S., & Ayoub, F. (2016). Resolving Fine-Scale Heterogeneity of Co-Seismic Slip and the Relation to Fault Structure. *Scientific Reports*, 6, 27201.
- Molnar, P. (2012). Isostasy can't be ignored. *Nature Geoscience*, 5(2), 83–83.
- Molnar, P., & England, P. (1990). Late Cenozoic uplift of mountain ranges and global climate change: chicken or egg? *Nature*, 346(6279), 29–34.
- Muenchow, J., Brenning, A., & Richter, M. (2012). Geomorphic process rates of landslides along a humidity gradient in the tropical Andes. *Geomorphology*, 139–140, 271–284.
- Okada, Y. (1992). Internal Deformation Due to Shear and Tensile Faults in a Half-Space. *Bulletin of the Seismological Society of America*, 82(2), 1,018–1,040.
- Parker, R. N., Densmore, A. L., Rosser, N. J., de Michele, M., Li, Y., Huang, R. Q., et al. (2011). Mass wasting triggered by the 2008 Wenchuan earthquake is greater than orogenic growth. *Nature Geoscience*, 4(7), 449–452.
- Parker, R. N., Hancox, G. T., Petley, D. N., Massey, C. I., Densmore, A. L., & Rosser, N. J. (2015). Spatial distributions of earthquake-induced landslides and hillslope preconditioning in the northwest South Island, New Zealand. *Earth Surface Dynamics*, 3(4), 501–525.
- Perron, J. T. (2017). Climate and the Pace of Erosional Landscape Evolution. *Annual Review of Earth and Planetary Sciences*, 45(1), 561–591.
- Raymo, M. E., Ruddiman, W. F., & Froelich, P. N. (1988). Influence of late Cenozoic mountain building on ocean geochemical cycles. *Geology*, 16(7), 649–653.
- Ren, Z., Zhang, Z., Zhang, H., Zheng, W., & Zhang, P. (2018). The Role of the 2008  $M_w$  7.9 Wenchuan Earthquake in Topographic Evolution: Seismically Induced Landslides and the Associated Isostatic Response. *Tectonics*, 37, 2748–2757. <https://doi.org/10.1029/2017TC004848>
- Savage, J. C. (1983). A dislocation model of strain accumulation and release at a subduction zone. *Journal of Geophysical Research*, 88(B6), 4984–4996.
- Savage, J. C., & Gu, G. (1985). A plate flexure approximation to postseismic and interseismic deformation. *Journal of Geophysical Research*, 90(B10), 8,570–8,580.
- Scheingross, J. S., Minchew, B. M., Mackey, B. H., Simons, M., Lamb, M. P., & Hensley, S. (2013). Fault-zone controls on the spatial distribution of slow-moving landslides. *GSA Bulletin*, 125(3–4), 473–489.
- Scholz, C. H. (2002). *The Mechanics of Earthquakes and Faulting* (2nd ed.p. 471). Cambridge, U.K: Cambridge University Press.
- Scholz, C. H., & Campos, J. (2012). The seismic coupling of subduction zones revisited. *Journal of Geophysical Research*, 117, B05310. <https://doi.org/10.1029/2011JB009003>
- Simpson, G. (2014). Decoupling of foreland basin subsidence from topography linked to faulting and erosion. *Geology*, 42(9), 775–778.
- Simpson, G. (2015). Accumulation of permanent deformation during earthquake cycles on reverse faults. *Journal of Geophysical Research: Solid Earth*, 120, 1958–1974. <https://doi.org/10.1002/2014JB011442>
- Stevens, V. L., & Avouac, J. P. (2015). Interseismic coupling on the main Himalayan thrust. *Geophysical Research Letters*, 42, 5828–5837. <https://doi.org/10.1002/2015GL064845>
- Stein, R. S., King, G. C. P., & Rundle, J. B. (1988). The growth of geological structures by repeated earthquakes 2: field examples of continental dip-slip faults. *Journal of Geophysical Research*, 93(B11), 13,319–13,331.
- Stirling, M., McVerry, G., Gerstenberger, M., Litchfield, N., van Dissen, R., Berryman, K., et al. (2012). National Seismic Hazard Model for New Zealand: 2010 UpdateNational Seismic Hazard Model for New Zealand: 2010 Update. *Bulletin of the Seismological Society of America*, 102(4), 1514–1542. <https://doi.org/10.1785/0120110170>
- Sun, T., Wang, K., Iinuma, T., Hino, R., He, J., Fujimoto, H., et al. (2014). Prevalence of viscoelastic relaxation after the 2011 Tohoku-oki earthquake. *Nature*, 514(7520), 84–87. <https://doi.org/10.1038/nature13778>
- Tanyaş, H., van Westen, C. J., Allstadt, K. E., Anna Nowicki Jessee, M., Görüm, T., Jibson, R. W., et al. (2017). Presentation and Analysis of a Worldwide Database of Earthquake-Induced Landslide Inventories. *Journal of Geophysical Research: Earth Surface*, 122, 1991–2015. <https://doi.org/10.1002/2017JF004236>
- Tapponnier, P., Zhiqin, X., Roger, F., Meyer, B., Arnaud, N., Wittlinger, G., & Jingsui, Y. (2001). Oblique Stepwise Rise and Growth of the Tibet Plateau. *Science*, 294(5547), 1,671–1,677.

- Thatcher, W., & Rundle, J. B. (1984). A viscoelastic coupling model for the cyclic deformation due to periodically repeated Earthquakes at subduction zones. *Journal of Geophysical Research*, 89(B9), 7631–7640.
- Theunissen, T., Font, Y., Lallemand, S., & Liang, W.-T. (2010). The largest instrumentally recorded earthquake in Taiwan: revised location and magnitude, and tectonic significance of the 1920 event. *Geophysical Journal International*, 183(3), 1119–1133.
- Torres, M. A., West, A. J., & Li, G. (2014). Sulphide oxidation and carbonate dissolution as a source of CO<sub>2</sub> over geological timescales. *Nature*, 507(7492), 346–349.
- Vanmaercke, M., Ardizzone, F., Rossi, M., & Guzzetti, F. (2017). Exploring the effects of seismicity on landslides and catchment sediment yield: An Italian case study. *Geomorphology*, 278, 171–183.
- Vergne, J., Cattin, R., & Avouac, J. P. (2001). On the use of dislocations to model interseismic strain and stress build-up at intracontinental thrust faults. *Geophysical Journal International*, 147(1), 155–162.
- Vita-Finzi, C. (2000). Deformation and seismicity of Taiwan. *Proceedings of the National Academy of Sciences*, 97(21), 11,176–11,180.
- Wang, H., Liu, M., Shen, X., & Liu, J. (2010). Balance of seismic moment in the Songpan-Ganze region, eastern Tibet: Implications for the 2008 Great Wenchuan earthquake. *Tectonophysics*, 491(1), 154–164.
- Wang, J., Jin, Z., Hilton, R. G., Zhang, F., Densmore, A. L., Li, G., & West, A. J. (2015). Controls on fluvial evacuation of sediment from earthquake-triggered landslides. *Geology*, 43(2), 115–118.
- Watts, A. B. (2001). *Isostacy and flexure of the lithosphere*. Cambridge: Cambridge University Press.
- Wells, D. L., & Coppersmith, K. J. (1994). New Empirical Relationships among Magnitude, Rupture Length, Rupture Width, Rupture Area, and Surface Displacement. *Bulletin of the Seismological Society of America*, 84(4), 974–1002.
- Wesnousky, S. G. (1988). Seismological and structural evolution of strike-slip faults. *Nature*, 335, 340.
- Wesnousky, S. G. (1994). The Gutenberg-Richter or characteristic earthquake distribution, which is it? *Bulletin of the Seismological Society of America*, 84(6), 1940–1959.
- Whipple, K. X. (2009). The influence of climate on the tectonic evolution of mountain belts. *Nature Geoscience*, 2(2), 97–104.
- Whipple, K. X., Shirzaei, M., Hodges, K. V., & Ramon Arrowsmith, J. (2016). Active shortening within the Himalayan orogenic wedge implied by the 2015 Gorkha earthquake. *Nature Geoscience*, 9, 711.
- Wolman, M. G., & Miller, J. P. (1960). Magnitude and Frequency of Forces in Geomorphic Processes. *The Journal of Geology*, 68(1), 54–74.
- Xu, C., Xu, X., Yao, X., & Dai, F. (2014). Three (nearly) complete inventories of landslides triggered by the May 12, 2008 Wenchuan M<sub>w</sub> 7.9 earthquake of China and their spatial distribution statistical analysis. *Landslides*, 11(3), 441–461.
- Xu, X., Wen, X., Yu, G., Chen, G., Klinger, Y., Hubbard, J., & Shaw, J. (2009). Coseismic reverse- and oblique-slip surface faulting generated by the 2008 Mw 7.9 Wenchuan earthquake, China. *Geology*, 37(6), 515–518.
- Yanites, B. J., Tucker, G. E., Mueller, K. J., & Chen, Y. G. (2010). How rivers react to large earthquakes: Evidence from central Taiwan. *Geology*, 38(7), 639–642.
- Zhang, P.-Z., Shen, Z., Wang, M., Gan, W., Bürgmann, R., Molnar, P., et al. (2004). Continuous deformation of the Tibetan Plateau from global positioning system data. *Geology*, 32(9), 809–812. <https://doi.org/10.1130/G20554.1>
- Zhang, S., Zhang, L. M., & Glade, T. (2014). Characteristics of earthquake- and rain-induced landslides near the epicenter of Wenchuan earthquake. *Engineering Geology*, 175, 58–73.